A planar-sheet nongraphitic zero-bandgap sp^2 carbon phase made by the low-temperature reaction of γ-graphyne

Ali E. Aliev[a], Yongzhe Guo[b], Alexandre F. Fonseca[c], Joselito M. Razal[d], Zhong Wang[a], Douglas S. Galvão[c], Claire M. Bolding[e], Nathaniel E. Chapman-Wilson[e], Victor G. Desyatkin[e], Johannes E. Leisen[f], Luiz A. Ribeiro Junior[g], Guilherme B. Kanegae[c], Peter Lynch[d,h], Jizhen Zhang[d,h], Mia A. Judicpa[d,h], Aaron M. Parra[a], Mengmeng Zhang[a], Enlai Gao[b], Lifang Hu[i], Valentin O. Rodionov[e,1], and Ray H. Baughman[a,1]

The highest sheet symmetry form of graphyne, with one triple bond between each neighboring hexagon in graphene, irreversibly transforms exothermically at ambient pressure and low temperatures into a nongraphitic, planar-sheet, zero-bandgap phase consisting of intrasheet-bonded sp^2 carbons. The synthesis of this sp^2 carbon phase is demonstrated, and other carbon phases are described for possible future synthesis from graphyne without breaking graphyne bonds. While measurements and theory indicate that the reacting graphyne becomes nonplanar because of sheet wrinkling produced by dimensional mismatch between reacted and nonreacted sheet regions, sheet planarity is regained when the reaction is complete. Although the observed elimination of triple bonds to make parallel planar sp^2 carbon sheets likely requires ordered transformation within each sheet, diffraction data for reacted multisheet stacks indicate that the relative lateral positions of neighboring sheets are disordered, as predicted, since no crystalline diffraction peak (other than for the intersheet spacing) is observed.

graphyne | carbon phases | zero-bandgap carbon | planar-sheet nongraphitic sp^2 carbons | applications of planar-sheet carbons

The structure and properties of periodic carbon phases containing aromatic rings separated by triple bonds were predicted in 1987 by Baughman, Eckhardt, and Kertesz (1), and oligomers were later made by Haley (2, 3), Diederich (4, 5), and collaborators. The two most symmetric such carbon sheet structures were synthesized, which contain the aromatic rings in graphene separated from neighboring aromatic rings by solely only one acetylene or one diacetylene group. For simplicity, we here call these structures graphyne and graphdiyne, rather than the more precise γ-graphyne and γ-graphdiyne. Zhu's group (6) first synthesized graphdiyne. There have been numerous efforts to synthesize graphyne (7), and the method we will use is the irreversible Sonogashira coupling of Rodionov's teams (8).

We here make an sp^2 carbon phase by heating the previously described graphyne (8) at ambient pressure from above ~160 to ~310 °C. Various sp^2 carbon phases have been proposed by Hoffman et al. (9) and by Belenkov and Ali-Pasha (10), including all-sp^2 carbon phases theoretically derived by complete intersheet reaction of the triple bonds in graphyne and graphdiyne to form polyacetylene chains. Possible high-pressure transformation products were proposed for graphyne (11, 12) and graphdiyne (13) that additionally involve benzene ring coupling into a lonsdaleite-diamond (11) or helical configuration (12). However, the sole experimental evidence for a phase transformation was from Raman spectroscopy during diamond-pressure-cell graphdiyne compression, where a phase transition started at ~5.2 GPa (14), and the thermal or laser-produced heating of graphyne (8). This pressure-induced graphdiyne transformation reportedly results from irreversible intersheet sp bond to sp^2 bond conversion, which ends by ~13 GPa (14).

Little was known about graphyne's ambient-pressure thermal transformation (8), except that it irreversibly decreases the quantity of sp carbons. New measurements are described for this transformation and compared with new predictions for low-energy sp-free and low-sp content phases that might result. Two transformation types are considered. The first is polyacetylene chain formation by intersheet triple bond reaction, and the second is an intrasheet reaction that converts all sp carbons to sp^2 ring carbons. We show that this low-temperature reaction at ambient pressure is intrasheet. The product is a planar-sheet zero-bandgap sp^2 carbon phase that was neither experimentally nor theoretically known.

Results

Synthesis and Characterization of ^{13}C-Labeled Graphyne.
The synthesis and characterization of the precursors used to make graphyne with ^{13}C-labeled acetylene groups are described in *SI Appendix* and in associated *SI Appendix, Figs. S1–S7*. Nuclear

magnetic ^{13}C spectroscopy results for graphyne containing the ^{13}C-labeled acetylene groups before and after thermal annealing are in *SI Appendix*, Figs. S8 and S9, respectively. Characterization of impurities in graphyne is in *SI Appendix*, Figs. S10–S15.

Measurements for Graphyne's Transition. Differential scanning calorimetry (DSC) shows that the investigated graphyne has a large exothermic transformation (*Top* panel of Fig. 1*A*). This transformation varies in temperature, likely depending on graphyne perfection, but is typically detected between 160 and 310 °C, with a heat-release peak between 250 and 280 °C. The transition heat varied from ~0.45 to ~0.55 kJ/g, depending upon the graphyne synthesis run. Heating graphyne at 5 °C/min from RT to 305 °C produces ~3% weight loss and further heating to 600 °C provides 43% additional weight loss (*SI Appendix*, Fig. S16). Measurements between 150 and 350 °C provided evidence of C_6H_5Br emission, by likely decomposition of groups on graphyne sheet edges (*SI Appendix*, Figs. S10–S14).

The lower Fig. 1*A* panels are RT measurements for gradually annealed samples. The top three Fig. 1*A* panels and Fig. 1 *B* and *C* show that the exothermic DSC transition occurs at temperatures where decreases occur in infrared absorbance due to internal (2,193 cm^{-1}) and terminal triple bonds (2,110 cm^{-1}) and in the Raman peak intensity from internal triple bonds. Since the Raman scattering requires strong laser excitation, that might overheat the sample, all measurements were conducted at a low beam power of 0.2 mW (*SI Appendix*, Fig. S17), which did not affect the intensity of triple-bond peak during 120-min excitation (*SI Appendix*, Fig. S17 and S18). *SI Appendix*, Fig. S19 shows the room temperature IR absorbance spectra for graphyne that was annealed for an hour at progressively increased higher temperatures. The red shift of the plasmonic edge shown by the dashed arrow line in *SI Appendix*, Fig. S19 is responsible for the derived band gap in Fig. 1*A* (*Bottom* panel).

Evidence for complete conversion of sp carbons to sp^2 carbons by heating to 325 °C was obtained by ^{13}C NMR measurements (*SI Appendix*, Figs. S8 and S9) on thermally annealed graphyne in which all sp carbons were ^{13}C labeled (*SI Appendix*,
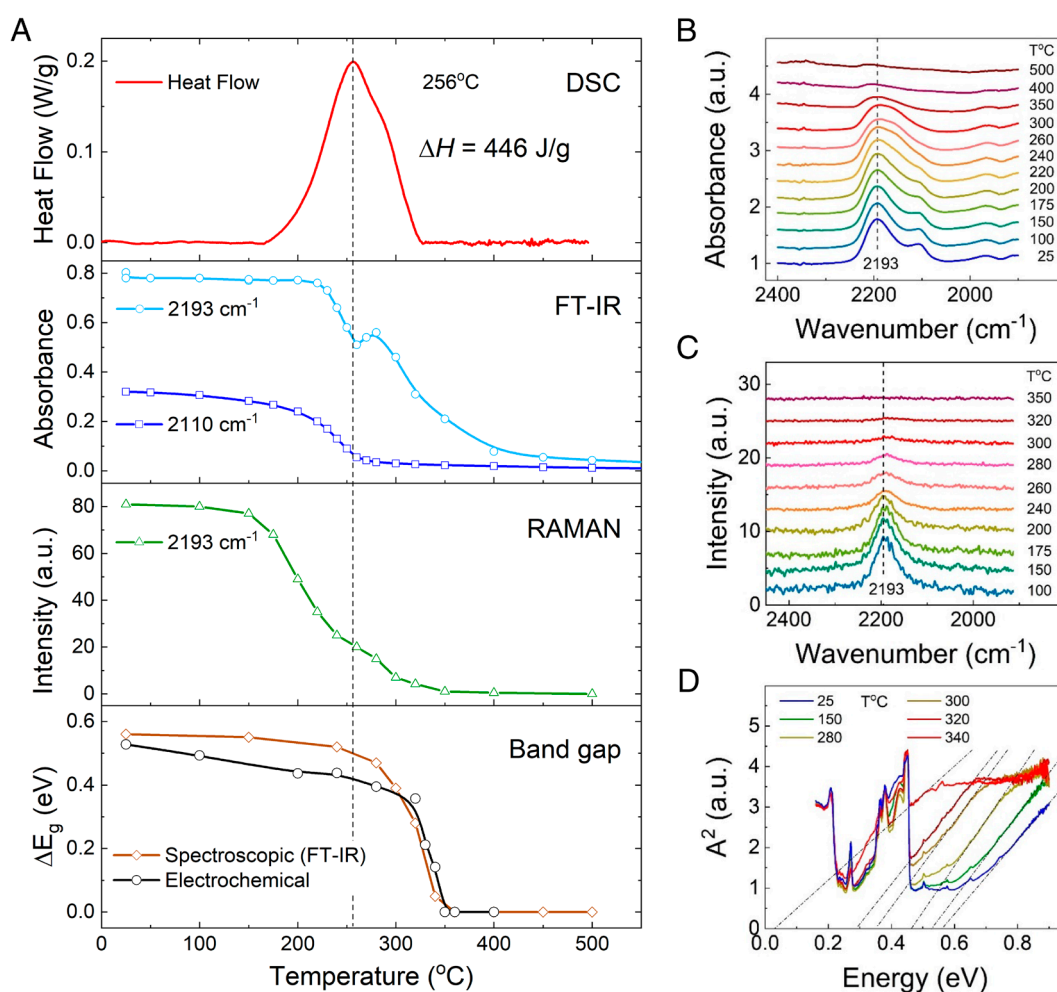
Fig. 1. DSC, spectroscopic, and electrochemical indication of the thermal transformation of graphyne. (*A*) The DSC-measured temperature dependence of exothermic heat flow above nearby pretransition and posttransition heat flows, using 2 °C/min heating in N_2 (*Top* panel) and the annealing temperature dependence of 1) the FT-IR absorption for internal and terminal triple bonds (second panel); 2) the Raman triple bond intensity using low-power 532 nm excitation (third panel); and 3) the average band gaps obtained using a Tauc plot (15) of absorbed energy (brown curve) and obtained electrochemically (black curve), as described in the text (fourth panel). The second average bandgap estimate in this fourth panel was obtained from *SI Appendix*, Fig. S21, which is from potential scans like in *SI Appendix*, Fig. S20. The wavenumbers of internal and terminal triple bonds were 2,193 cm^{-1} and 2,110 cm^{-1}, respectively. The FT-IR absorption (*B*) and Raman spectra (*C*) used to obtain the results in the second and third panels of (*A*), respectively, are shifted vertically for clarity. (*D*) The pictured Tauc plot method was used to obtain the results in the fourth panel of (*A*) from the absorbance spectra obtained after progressively higher temperature anneals (*SI Appendix*, Fig. S18). The results in (*B–D*) and *SI Appendix*, Fig. S18 were conducted at RT after step-by-step heating the initially unreacted graphyne in 0.1 mTorr vacuum for 1 h at the indicated progressively higher temperatures.

Figs. S1–S9). A significant decrease in the T_1 relaxation time for the labeled nuclei was observed, suggesting that either the material's surface became more accessible to ambient oxygen, the material's crystallinity decreased, or both factors were at play.

The bottom Fig. 1*A* panel alternatively uses the Tauc (15) absorption plots of Fig. 1*D* or an electrochemical method (*SI Appendix,* Figs. S20 and S21) to obtain the average bandgap. The latter annealing temperature dependence of average bandgap resulted from normalizing the ratio of redox peak height to CV capacitance, so that the redox-peak-separation bandgap of nonannealed graphyne was obtained at 25 °C. This capacitance normalization is needed because the diffraction-confirmed transitory sheet wrinkling during transformation (Fig. 2) increases the available area for double layer and Faradaic processes. Both bottom panel bandgaps completely vanish during annealing to ~350 °C. Our previous redox-peak-separation and Tauc plot bandgaps for graphyne were 0.47 eV and 0.48 eV (8), respectively, which are close to those for the presently used graphyne sample (0.52 eV and 0.56 eV). Due to the small graphyne amount made in each synthesis run (300 mg or smaller), each sample investigated in Fig. 1*A* was from a different batch, and we know this can influence the phase transition.

DSC measurements revealed surprising transformation kinetics. A graphyne sample was first heated in the DSC from 25 °C to a low temperature (150 °C) within the exotherm range, annealed for an hour at this temperature, and then naturally cooled back to RT, before this whole process was conducted during the next scans from 25 °C to successively higher annealing temperatures (*SI Appendix,* Fig. S22). Little or no exotherm occurred until reaching the previous annealing temperature, and then, it largely stopped when the targeted new constant annealing temperature was reached. This behavior suggests that regions of reacting graphyne transform when their local free-energy change becomes near zero, like for the free-energy-driven melting of a mixture of non-melt-miscible particles. *SI Appendix,* Fig. S22 shows the close

correlation between these results and the heat flow during uninterrupted heating of this graphyne sample at 2 °C/min.

Transmission electron microscope images (*SI Appendix,* Fig. S23*A*) indicate that the lateral size of individual graphyne sheet stacks is not much larger than about 300 nm. *SI Appendix,* Fig. S23*B* shows the electron diffraction pattern for these individual sheet stacks, which is the same as previously reported in our publication on the synthesis of the presently used graphyne (8). *SI Appendix,* Fig. S23*C* shows a SEM microscope image of a typical large graphyne particle, which is a poorly orientationally ordered aggregate of an enormous number of individual thin graphyne plate stacks.

Synchrotron diffraction measurements were conducted in situ versus temperature on graphyne deposited on a stationary flat plate, as well as at RT for a continuously rotated capillary-packed sample. The latter agrees with our previous rotating capillary results for graphyne (8) and with the theoretically predicted cell parameters (*SI Appendix,* Table S1). Because of stacking faults, only $(h,k,0)$ reflections and a strong intersheet reflection were observed. Due to the preferred orientation and the high intensity of this reflection (observed in both flat-plate substrate and rotating capillary powder measurements), only the intersheet reflection was seen in nonrotating flat-plate-substrate powder diffraction.

The diffraction intensity of graphyne's interlayer spacing progressively disappeared during heating to 172 °C, while its d-spacing little changed (Fig. 2). A new peak from the interlayer spacing of transformed graphyne begins to significantly appear at 264 °C and then dramatically increase intensity, decrease line-width, and slightly increase interlayer spacing during heating to 320 °C, where its d-spacing increased to 3.55 Å. This new diffraction peak was maintained and provided a small contraction to 3.51 Å during cooling to 50 °C.

The disappearance of the intersheet diffraction peak for reacting graphyne at between 165 and 172 °C and the progressive appearance of the interlayer peak for the thermal reaction product at
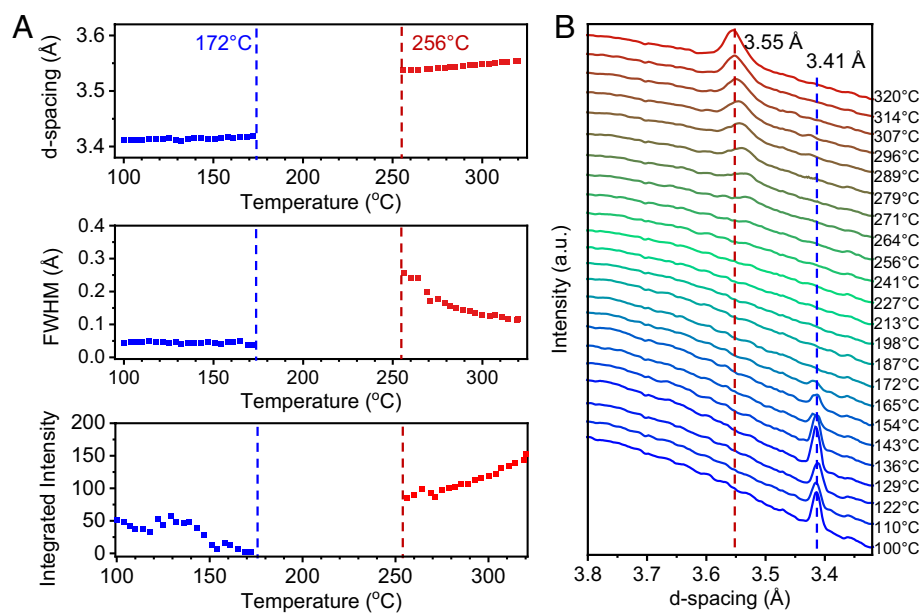
Fig. 2. Changes in intersheet diffraction lines measured in situ in a synchrotron, using 0.590 Å radiation, during thermal annealing of graphyne from 100 to 320 °C using 2 °C/min heating. (*A*) The intersheet d-spacing, its Full Width at Half Maximum (FWHM), and its integrated peak intensity as a function of the maximum temperature of thermal exposure during the temperature scan, when measured for graphyne powder on a nonrotated flat-substrate. The time for diffraction data collection during the thermal scan was ~2 min during which the sample temperature changed only about 4 °C. (*B*) The observed X-ray diffraction spectra for different peak annealing temperatures, in the d-spacing range where graphyne-related intersheet diffraction is observed. Little or no interplanar line intensity is seen between ~172 and ~256 °C, likely because sheet wrinkling, caused by intrasheet strain mismatch between reacted and nonreacted sheet areas, decreases the intensity of the interplanar spacing to near zero. When the transformation is sufficiently high that some planar reacted sheet regions can stack parallel because of increased unwrinkling, diffraction due to the reacted product phase increasingly appears. Since intersheet reaction by formation of polyene chains would decrease the interplanar spacing, this observed increase in d-spacing indicates that this thermal transformation is intrasheet.

above 264 °C is explained by large strains due to mismatch of the lateral sheet dimensions of reacted and unreacted sheet areas (*SI Appendix*, Table S5). These strains cause wrinkling of the initially planar sheet, which displaces sheet atoms out-of-plane, thereby dramatically decreasing the intersheet diffraction intensity. As the transformation progresses, the gradual elimination of this wrinkling enables the appearance and strengthening of the interplanar diffraction for the reacted graphyne. This diffraction intensity decreases very early in the transformation, before it is noticeable in DSC measurements, which is likely because only small reaction in each graphyne sheet is needed to disturb sheet planarity and since the heat of reaction per reacted sp carbon is initially reduced by associated intersheet and intrasheet strains.

Our diffraction measurements on the presently synthesized multisheet stacks of reacted graphyne do not show diffraction peaks other than the intense interlayer separation diffraction peak, likely because of the below discussed laterally disordered intersheet stacking. Note that the distorting effect on the interplane diffraction linewidth due to stacked fully reacted sheets by the wrinkling of partially reacted sheets in their proximity is suggested in Fig. 2*A* by the major decrease in the FWHM linewidth of the interplanar d-spacing diffraction peak as the maximum thermal annealing goes from 255 °C (where it is about 0.25 Å) to 320 °C (where it is about 0.12 Å). However, some of this linewidth decrease can result from the diffraction linewidth consequence of the increase in the number of fully ringized adjacent layers that are stacked together, rather than from their small distortion by nearby buckled sheets.

Possible Low-Energy Topochemical Graphyne Transformation Products and Their Comparison with Experiments. Since graphyne reacts at low temperatures (without external mechanical,

chemical, or radiation-induced initiation), we consider lower energy product structures that could form without rupturing any periodic bonds in graphyne. Transformations involving interlayer coupling of benzene rings by sp^3 carbons are not considered since the above experiments indicate that the transformed graphyne contains mostly sp^2 carbons.

Two graphyne transformation types are considered: intersheet acetylene group reaction and triple bond elimination by intraplane reaction. The products are called polyeneized graphyne and ringized graphyne, since the first results in interlayer polyene chains and the second produces new sp^2 intralayer carbon rings.

We first consider transformations to polyeneized graphyne, a possibility conceived when graphynes were first proposed (1). However, polyene chain formation from all graphyne triple bonds can occur only for graphyne having eclipsed sheets, which is not the lowest energy predicted stacking (*SI Appendix*, Fig. S24) or one observed for graphyne. We do not consider transformations having intersheet stresses so high that eclipsed phenyl rings covalently couple by forming sp^3 carbons. They are excluded since there is no sp^3 peak in our solid-state ^{13}C NMR spectra of reacted graphyne (*SI Appendix*, Fig. S9). Also, the Raman G band from aromatic groups initially increases three-fold during thermal transformation, rather than decreasing (*SI Appendix*, Figs. S17 and S18).

Intersheet transformations by triple bond reaction to form polyene chains must be topochemical, like for diacetylene solid-state polymerization (16). The only sheet stacking that provides both a lower predicted energy than the eclipsed structure (*SI Appendix*, Table S3) and the topochemical ability to enable 1,2-addition acetylene reaction is the AB1 stacking of *SI Appendix*, Fig. S24. Our earlier molecular dynamics (MD) calculations using ReaxFF force field (8) and present density functional theory

A	B ΔH = -0.257 kJ/g	C ΔH = -0.585 kJ/g
D ΔH = -0.241 kJ/g	E ΔH = -1.163 kJ/g	F ΔH = -1.275 kJ/g
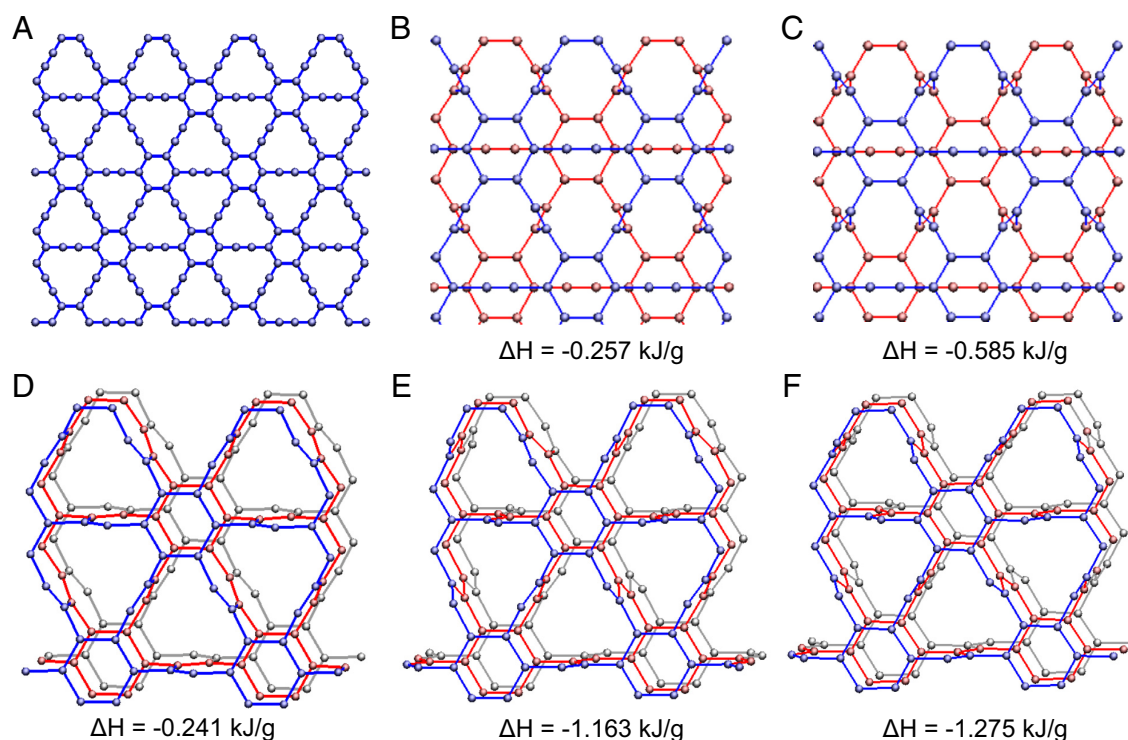
Fig. 3. The bond arrangements in nonreacted graphyne and graphyne intersheet reacted by formation of cis or trans polyacetylene chains. (*A*) a graphyne sheet; (*B*) 2-cis, 1-sp polygraphyne; (*C*) 2-trans, 1-sp polygraphyne; (*D*) 3-cis polygraphyne; (*E*) 1-cis, 2-trans polygraphyne; and (*F*) 3-trans polygraphyne. These views are orthogonal to the graphyne sheet plane and in approximately the same direction for the reacted graphyne. The bonds that connected atoms in successive sheets in the parent graphyne are colored blue, red, or gray, respectively, as the graphyne sheets recede into the distance, and the bonds formed by intersheet reaction are black. The enthalpy changes are from DFT calculations at 0 K (*SI Appendix*, Table S4). *SI Appendix*, Table S6 provides the calculated structural parameters for these phases.

(DFT) calculations at 0 K (*SI Appendix*) agree with previous predictions (17) that this structure has a lower energy than the eclipsed structure. However, even when graphyne is perfectly stacked as AB1 (*SI Appendix*, Fig. S24), only 2/3 of the acetylene groups can potentially react since 1/3 of the acetylene groups are between aromatic groups of neighboring sheets. The chain fraction whose propagation by interlayer reaction is blocked would be greatly increased when such intersheet interactions are only between nearest-neighbor sheets, and the next intersheet interactions are of the same type, but nonperiodic.

Intersheet graphyne polymerization is energetically most likely by reaction of acetylene group arrays to form up to three linked cis or trans polyacetylene chains per aromatic carbon ring, when double counting due to chain sharing between rings is avoided by assigning ½ to each connection. Hence, we call these polyeneized graphyne structures with favorable formation energies for low-temperature thermal generation 2-cis, 1-sp polygraphyne; 2-trans, 1-sp polygraphyne; 3-cis polygraphyne; 1-cis, 2-trans polygraphyne; and 3-trans polygraphyne, where a sp index of 1 indicates acetylenes with two connections to rings are unpolymerized. Fig. 3 *B* and *C* show that the polyacetylene chains in 2-cis, 1-sp polygraphyne and in 2-trans, 1-sp polygraphyne are far from planar. Hence, the chain is called cis or trans depending on whether the bonds formed by reaction are in cis or trans positions in the reacting acetylene group array.

DFT and MD calculations (18, 19) were conducted for all investigated polygraphyne and ringized graphyne structures. *SI Appendix,* Table S4 provides the predicted changes of phase enthalpies and the percentage changes in dimensions during the transition from graphyne to each polygraphyne in Fig. 3. The polygraphynes without completely polymerized acetylene groups are 2-cis, 1-sp polygraphyne and 2-trans, 1-sp polygraphyne, which are for the AB1 stacking mode that blocks the reaction of 1/3 of the acetylene groups. Diffraction results (8) show that the presently synthesized graphyne lacks long-range periodicity in intersheet stacking, so the extent of sp bond elimination by forming interlayer polyene chains is further restricted to be far below 2/3.

We next predict transformed structures for graphyne that is ringized by possibly a Bergman-like reaction (20). Various planar ringized nongraphitic sp^2 carbon phases have been theoretically described, like the pentagon and heptagon sheets of Crespi et al. (21), the pentagon, hexagon, and heptagon sheets of Terrones et al. (22), and the graphene allotropes of Enyaskin and Ivanovski (23). Ma et al. considered transformations of graphyne and graphdiyne at extreme temperatures to produce disordered carbon sheets by bond breaking (24). In contrast, our presented transformations provide all sp^2 carbon sheets without breaking bonds in the periodic graphyne structure. The only previously described (1, 25, 26) planar all-sp^2 carbon sheet that could potentially result from an in-plane reaction without bond rupture in graphyne is the biphenylene carbon of *SI Appendix*, Fig. S25E. However, we exclude this structure since group-increment-based results (1) and quantum chemical calculations (*SI Appendix,* Table S5) predict that its single sheet formation energy is higher than graphyne.

We found four ringene all sp^2 carbon phases with lower enthalpies than graphyne, which could theoretically form by in-plane reaction of graphyne without graphyne bond breaking. These favorable formation enthalpy reactions result from the transformation of sp carbons into sp^2 carbons within larger rings, rather than being exclusively in 4-carbon rings. According to the number of carbons in the rings formed during intrasheet reaction, the ringized sheet structures (Fig. 4) are called 5,6,9 ringene; 4-9 ringene; 4-9 double ringene; and 4-8 ringene. While we have found many other in-plane reacted structures that could conceivably form by eliminating all of graphyne's triple bonds without

breaking any of its periodic covalent bonds, the only structures we found that can do this while providing the experimentally observed planar fully reacted state are the above (except 4-9 ringene) and the below mentioned simple variants. This figure shows that the 5,6,9 ringene structure, which contains no 4-member rings, has the lowest enthalpy of formation from graphyne at 0 K (–1.84 kJ/g). However, this most favorable formation enthalpy does not necessarily imply that this structure is the reaction product, since the reaction product might be kinetically derived, rather than thermodynamically determined.

Discussion

We could experimentally detect only sp^2 carbons in the transformed graphyne. If graphyne's thermal transformation exclusively occurred by intersheet acetylene polymerization, only a fraction of the acetylene groups could polymerize unless graphyne sheets predominately stack eclipsed, which is neither energetically favored nor observed. Complete intersheet acetylene reaction providing polyene chains is further excluded since it provides large predicted percent contractions in intersheet spacing (–21.6 to –26.1% and –22.6 to –24.2% from 0 K DFT and MD calculations, respectively, in *SI Appendix,* Table S4). If complete reaction occurred by combined intrasheet ring formation and intersheet polyene formation (*SI Appendix*, Fig. S26), large contractions in the intersheet spacing are still predicted (–15.3 and –19.1% for the cis-chain and trans-chain structures, respectively), although only 20% of the triple bonds react intersheet. These results disagree in sign and size with the small diffraction-measured interplanar spacing expansion produced by complete reaction, where the spacing of the reacted graphyne is 2.93% larger than for the nonreacted graphyne at 100 °C. This small observed increase in interplanar spacing during in-plane reaction is reasonable because of the increase in areal sheet density and the likely non-energy-minimized relationship between nearest-neighbor sheets produced by in-plane reaction.

However, we have not yet found a way to fully exfoliate either graphyne or thermally transformed graphyne into single sheets. This poses a problem since we consequently do not have the present ability to experimentally prove by electron diffraction measurements that individual reacted sheets are highly ordered. Disorder in the lateral orientation of neighboring sheets arises because a) the reaction direction in these sheets differs since it depends on the location of reaction initiation and b) additional lateral sheet disorder in intersheet stacking is expected because of sheet wrinkling and dewrinkling during reaction. Equilibration to obtain ordered intersheet stacking cannot be obtained at lower annealing temperatures than the ringene degradation temperature because of the structural complexity of ringene phases and the resulting small energy decrease driving ordered stacking. This lateral disorder in sheet stacking means that only the intense (001) intersheet diffraction peak will appear. Until the graphyne synthesis method is dramatically improved, so that impurities deposited on the graphyne surface are eliminated or methods to remove these contaminants are developed, powerful nanoscale imaging methods cannot be usefully deployed for experimental confirmation of the reacted graphyne's sheet structure.

These results indicate that the large DSC-observed exotherm arises from intrasheet transformation of sp carbons of graphyne to sp^2 ring carbons. Fig. 1 shows that the large DSC-measured temperature range of the exothermic transformation coincides with the temperature range where a large fraction of the FT-IR triple-bond absorbance disappears and essentially all of the Raman
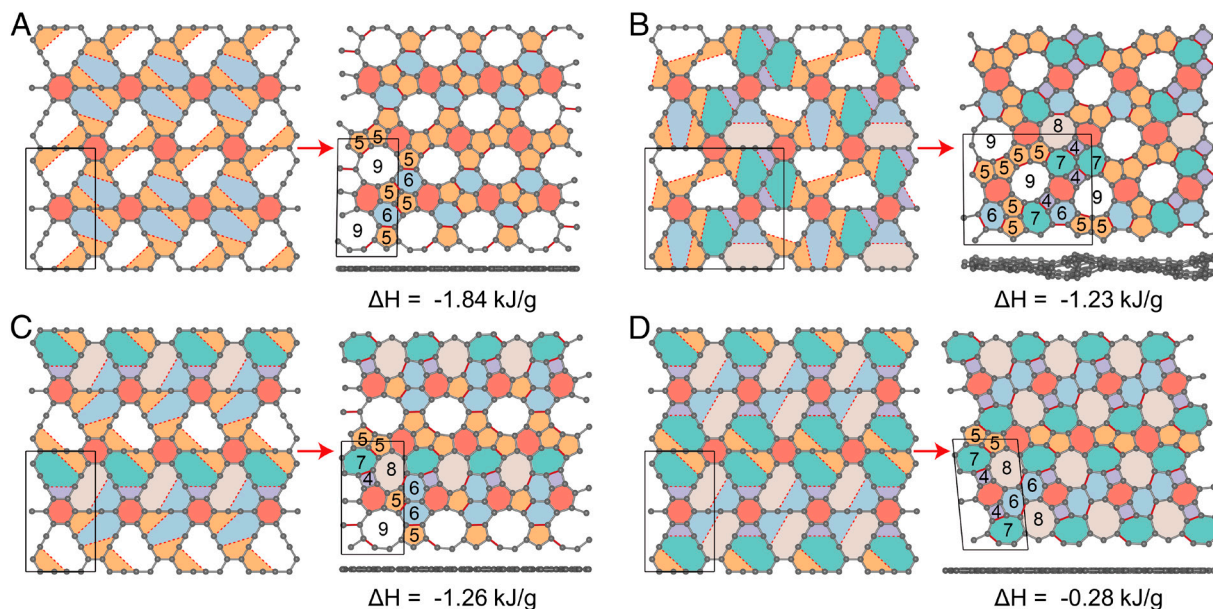
Fig. 4. The bond connections between parent sp carbons potentially made during in-plane reaction of graphyne, without bond breaking, and the resulting all-sp² carbon structures. These transformations are for (*A*) 5,6,9 ringene, (*B*) 4-9 ringene, (*C*) 4-9 double ringene, and (*D*) 4-8 ringene. The red arrows in each part indicate the direction of the irreversible thermal transformation. The number of carbon atoms in each ring of the reacted structure is indicated at ring center, the unit cells of the products are shown, and a side view of each reacted sheet is provided below the orthogonal view of each reacted sheet. Differently colored areas usually indicate rings and ring reactions that result in different carbon-number rings, but 6-carbon rings in the original graphyne are red and those formed by reaction are light blue. The provided ΔH for each investigated reacted graphyne structure corresponds to the MD ReaxFF calculated difference in the theoretically calculated enthalpy of the in-plane reacted graphyne phase and unreacted graphyne at 0 K (*SI Appendix*, Table S5). The calculated structural parameters for these phases are in *SI Appendix*, Table S7.

triple-bond intensity disappears. Also, the absorption-based and electrochemical-based average bandgap changes occur in the exotherm's approximate temperature range.

Of the periodic in-plane-reacted reactions in Fig. 4, the most likely is 5,6,9 ringene, which has the most favorable 0 K-calculated enthalpy decrease compared to graphyne (–1.84 kJ/g). It is predicted to have the observed planar sheets (Fig. 2) and a zero bandgap (*SI Appendix*, Table S8), which agrees with experiments (Fig. 1*A*). The 4-9 ringene is excluded as the sole product because its calculated structure is nonplanar. The 4-9 double ringene and 4-8 ringene are excluded as the main product because their calculated bandgaps are 0.23 eV and 0.17 eV, respectively.

A quite similar 0 K enthalpy difference between 5,6,9 ringene and unreacted graphyne was obtained using MD (ReaxFF potential), DFT, and Quantum Espresso (QE) calculations (–1.84, –2.21, and –2.17 kJ/g, respectively). The QE-calculated heat capacities for these phases, which are valid only for temperatures below where reaction or later volatilization starts, are in *SI Appendix*, Fig. S27, as are the thereby calculated small temperature dependence of the enthalpy difference due to the integrated heat capacity difference. These results show that the calculated enthalpy differences between these phases at 0 K (from –1.84 to –2.21 kJ/g) should approximately equal the measured enthalpy change during the transition. However, the measured transition exotherm (~0.5 kJ/g) is smaller than calculated for two possible reasons: the weight percent of graphyne in the synthesized samples is unknown, and likely low (no higher than 66.4% based on EDX element analysis of *SI Appendix*, Fig. S15 and Table S2), and the enthalpy of the synthesized ringene will be slightly increased by the below discussed intrasheet disorder. It is also possible that the reacted graphyne's structure is kinetically determined, rather than thermodynamically determined, so the heat of reaction might be much lower than for the most enthalpically favored structure.

Note that the labeled G and D bands in the Raman spectra of graphyne look nearly identical to peaks in the same spectral region

for largely acetylene-free thermally annealed graphyne (*SI Appendix*, Fig. S17*A*), despite the complex structure changes needed to eliminate graphyne's triple bonds by in-plane reaction. In order to show that a planar sp² hydrocarbon containing 5 and 6 carbon rings can provide similar Raman vibrations to those observed for reacted graphyne, we compare the observed Raman peaks of reacted graphyne at RT with those for solid fluoranthene (which contains only 5 and 6 carbon rings and is resonance stabilized like our in-plane-reacted graphyne). Although fluoranthene (after thermal annealing to remove impurities) has much narrower Raman peak widths than observed for reacted graphyne, it provides RT peaks at 1,612 and 1,455 cm⁻¹ (27). These results are reasonably consistent with observations for thermally annealed graphyne, which has Raman vibration peaks at 1,582 and 1,360 cm⁻¹ (*SI Appendix*, Fig. S17*A*). Moreover, the extremely broad vibration at 1,360 cm⁻¹ in reacted graphyne might arise from the superposition of a sharp vibration at about 1,455 cm⁻¹ (like in fluoranthene) and a possibly much stronger broad D band derived from disordered groups at sheet edges in nonreacted graphyne.

While the two-dimensionally periodic models of Fig. 4 show how periodic in-plane reaction can occur to eliminate essentially all triple bonds, transmission electron diffraction measurements on multilayer fully reacted graphyne plates show only diffuse scattering. This lack of (*h,k,0*) reflections in the transformed multilayer graphyne is not surprising, even when it is recognized that topochemical in-plane reaction must be occurring to produce each of the observed planar sp² sheets. The key point is that reaction in an individual sheet is equally likely to occur in any of the three crystallographically equivalent in-plane graphyne directions. Since the energy driving intersheet equilibration in lateral positioning is small, the structures equilibrated are long and quite complex, and the annealing temperatures that can be applied are low, the equilibration needed to provide intersheet order in lateral sheet position cannot be obtained. Also, note that the two most enthalpically favorable products are structurally related in the in-sheet-plane reaction direction. Fig. 4 shows that 5,6,9 ringene

reaction becomes the slightly less enthalpically favorable 4-9 ringene reaction when formation of a single 4-member carbon ring occurs for one-sixth of the phenyl rings in the original graphyne plane. Hence, intrasheet disorder would be introduced if these 4-member rings are introduced in the reaction direction less periodically than in 4-9 ringene. Nevertheless, the 5,6,9 ringene zigzag chains of graphyne-derived phenyl fused on opposite sides by two fused five-member rings are expected for the Fig. 4 models and for these less periodic variants.

Despite this absence of structural periodicity in sheet stacking, the experimentally observed planarity and zero bandgap of the graphyne reaction product is noteworthy for applications, especially if graphyne synthesis can be inexpensively upscaled. While Toh et al. recently reported (28) the exciting laser-assisted synthesis of free-standing sp^2 carbon monolayers containing five-to-eight member rings, they were amorphous and the center-to-center separation between neighboring stacked sheets was about 6 Å. There are clearly important properties and applications worlds to be explored for the present graphyne reaction product and its graphyne precursor, especially for their doped compositions. It will also be interesting to explore ways the present structural transformation of graphyne can be usefully modified by applied stresses and other means to provide other new phases, whose structures and energies are calculated here. Also, it will be interesting to explore various modifications of our synthesis method that might increase order in intersheet stacking, such as initiating in-plane graphyne reaction in one direction for all sheets by using thermal, radiation, or chemical initiation perpendicular to the desired reaction propagation direction.

Materials and Methods

Materials. All reagents and solvents were acquired from commercial suppliers (Acros Organics, Sigma-Adrich, TCI Chemicals, Fisher Scientific, Oakwood Chemical, and VWR International) and used without further purification, unless otherwise noted. Tetrahydrofuran (THF) was distilled over Na/benzophenone. Triethylamine (TEA) was distilled over CaH_2. Anhydrous pyridine (Py) was purchased from Acros in AcroSeal packaging and used without further purification.

Synthetic Methods. Reactions were monitored by thin-layer chromatography (TLC) carried out on 0.25 mm MilliporeSigma aluminum-backed silica gel plates (60F-254). Plates were visualized using 254 nm UV light and basic potassium permanganate stain (1.5 g $KMnO_4$, 0.5 g NaOH, and 10 g K_2CO_3 in 150 mL water; terminal alkynes stain yellow). Flash chromatography was performed on Luknova SuperSep™ (230 to 400 mesh) silica gel. Reactions requiring anhydrous or air-free conditions were performed under positive Ar pressure using standard Schlenk line techniques.

NMR Spectrometry. Routine NMR spectra were recorded on a Bruker Avance III HD 500 spectrometer operating at 500.24 (^{1}H), 125.79 (^{13}C) MHz and equipped with a Bruker Ascend 500 MHz US Narrow Bore Magnet and Broadband Prodigy TCI CryoProbe. NMR chemical shifts are reported in parts per million (ppm) and are calibrated against residual solvent signals of $CDCl_3$ (^{1}H δ 7.26, ^{13}C δ 77.16) and DMSO-d6 (^{1}H δ 2.5, ^{13}C δ 39.52). The following abbreviations are used to describe signal multiplicities: s–singlet, d–doublet, t–triplet, dd–doublet of doublets. The values of the spin–spin interaction constants (J) are provided in hertz (Hz).

GC–MS and EI–MS. GC–MS (gas chromatography–mass spectrometry) and EI–MS (electron ionization mass spectrometry) analyses were performed on an Agilent 7890B/5977B GC/MSD instrument equipped with an Agilent 7890B automatic liquid sampler, Agilent G4381A Thermal Separation Probe (TSP), and a 30 m × 0.25 mm DB-5MS capillary column (with 25-μm film thickness). Liquid samples (typically 1 μL) were introduced to the column via split mode injection with a 50:1 split ratio. The temperatures of the injection port (220 °C), MSD (Mass Selective Detector) transfer line (280 °C), MS source (230 °C), and MS quad (150 °C) were set, and the electron ionization energy used for the MS was 69.9 eV. The oven temperature was set at an initial temperature of 60 °C for 2.25 min, then ramped to 225 °C at 35°C min^{-1} and held at this final temperature for 3 min. The system deployed He gas flowing at 3.0 mL min^{-1} as the mobile phase. The method used

a 3 min solvent delay. Solid samples were introduced into the instrument using the TSP. After the TSP was preheated to the set temperature, the sample carrier was inserted into the probe, which was connected directly to the MSD transfer line by a deactivated quartz capillary. Data analysis was performed using Agilent MassHunter Qualitative Analysis Navigator.

The graphyne samples were positioned within a preheated Thermal Separation Probe (29), set to temperatures ranging between 150 and 400 °C. The TSP was directly linked to a quadrupole mass spectrometer via a brief deactivated capillary column. No identifiable fragments were observed in the obtained data for set temperatures below 200 °C. However, from 200 °C onward, the predominant species in the mass spectra consistently matched bromobenzene. This identification was confirmed by the presence of molecular ions C_6H_5Br at 156 and 158 m/z, along with the C_6H_5 peak at 77 m/z resulting from the loss of Br. These findings suggest that the transformation of graphyne initiates at sheet edges, involving significant skeletal rearrangement and C–C bond breaking at sheet edges even at relatively mild temperatures. The infrared spectroscopy observations, indicating the conversion of terminal alkynes before affecting internal alkynes, align with the results of the TSP–MS experiment. These results suggest that graphyne with a negligible fraction of triple bonds in terminal positions at internal or external sheet edges might have greatly enhanced thermal stability. In fact, it seems possible that more defect-free graphyne might not display the present structural transformation.

Infrared Spectroscopy. Routine small-molecule FTIR spectra were collected on an Agilent Cary 630 FTIR instrument equipped with a single-reflection germanium attenuated total reflectance module. The instrument was calibrated before sampling against a newly cleaned (acetone) and dried crystal surface. Solid samples were placed directly on the crystal and secured with a needle press. 512 scans from 4,000 to 600 cm^{-1} were recorded. A background was collected for each sample. The FT-IR spectra were collected using a PerkinElmer Spotlight 200i FTIR Microscopy System equipped with a Spectrum Two spectrometer capable of both transmittance and reflectance measurements in the mid-IR to near-IR range (600 to 7,800 cm^{-1}).

Thermogravimetric Analysis. The weight loss for graphyne was measured using a TA SDT Q600 thermal analyzer, which enables simultaneous measurement of weight change (TGA) and heat flow (DSC) from ambient temperature to 1,500 °C. In this study, the weight loss from 0 to 600 °C was measured at a 5 °C /min scan rate for 14.2 mg of graphyne powder filled into a 165.2 mg alumina ceramic pan. The heater chamber was continuously purged during the measurement with ultrapurified (99.99%) nitrogen gas at a flow rate of 50 mL/min.

Theoretical Methods. DFT and MD simulations were employed to study the formation energies and other properties, including dynamical tests of all polyneized and ringized structures, as well as pristine graphyne structures and their stacks. Unless otherwise mentioned, the DFT calculations were done with the Vienna Ab-Initio Simulation Package (30), and the MD simulations were performed using the LAMMPS package (18). During DFT calculations, the generalized gradient approximation of the Perdew–Burke–Ernzerhof functional (31) was used for the exchange and correlation interactions of electrons. For higher accuracy, the bandgaps of in-plane reacted structures were calculated at the hybrid HSE06 functional level (32). Considering the dispersion interactions, van der Waals corrections using the DFT-D3 (33) method were adopted in all calculations. An energy cutoff of 520 eV was used, and a k-point mesh with a density of about 50 Å was used for Brillouin zone sampling. All structures were fully relaxed using a conjugate gradient algorithm with a stringent convergence criterion of the force on each atom (10^{-2} eV Å^{-1}). For MD simulations, the state-of-the-art ReaxFF reactive force field (19) used two sets of parameters for simulating the interaction between the atoms within structures, one that is able to simulate hydrocarbons (34) and another that was developed for solid carbon (35). In *SI Appendix*, section 7, we present the formation energies and other properties of the structures considered in the present work.

MD energy minimizations were obtained for all structures with periodic boundary conditions (PBC) imposed along all directions in space (3D for stacks of graphynes and polyneized structures and 2D for pristine graphyne and ringized structures). The protocols for these calculations combined sets of energy minimization and free evolution dynamics algorithms to determine the lowest-energy structure, as suggested by Sihn et al. (36) and implemented by Kanegae and Fonseca (37) for determining the mechanical properties of graphyne families. Conjugate gradient and volume change methods provided by LAMMPS were used

to improve precision in the calculated structural energies. Thermal equilibration of the structures was also performed with PBC. Dynamical tests were performed with a fixed number of particles, by varying temperature and/or volume. Langevin thermostat and Nosé–Hoover thermostat and barostat were used when the structures were simulated with fixed volume and fixed pressure, respectively. In this last case, the volumes of the structures were allowed to change. Temperature damping factors were chosen to be 1.0 fs. Pressure-damping factors were chosen between 100 and 1,000 fs to decrease the oscillations caused by the algorithms of pressure convergence. Timesteps between 0.01 and 0.025 fs were considered.

Data, Materials, and Software Availability. All study data are included in the article and/or *SI Appendix*.

1. R. H. Baughman, H. Eckhardt, M. Kertesz, Structure-property predictions for new planar forms of carbon: Layered phases containing sp^2 and sp atoms. *J. Chem. Phys.* **87**, 6687–6699 (1987).
2. M. M. Haley, Synthesis and properties of annulenic subunits of graphyne and graphdiyne nanoarchitectures. *Pure Appl. Chem.* **80**, 519–532 (2008).
3. C. A. Johnson II, Y. Lu, M. M. Haley, Carbon networks based on benzocyclynes. 6. Synthesis of graphyne substructures via directed alkyne metathesis. *Org. Lett.* **9**, 3725–3728 (2007).
4. F. Diederich, All-carbon scaffolds by rational design. *Adv. Mater.* **22**, 803–812 (2010).
5. F. Diederich, Carbon scaffolding: Building acetylenic all-carbon and carbon-rich compounds. *Nature* **369**, 199–207 (1994).
6. G. Li *et al.*, Architecture of graphdiyne nanoscale films. *Chem. Commun.* **46**, 3256–3258 (2010).
7. J. Li, Y. Han, Artificial carbon allotrope γ-graphyne: Synthesis, properties, and applications. *Giant* **13**, 100140 (2023).
8. V. G. Desyatkin *et al.*, Scalable synthesis and characterization of multilayer γ graphyne, novel carbon crystals with a small direct bandgap. *J. Am. Chem. Soc.* **144**, 17999–18008 (2022).
9. R. Hoffman, T. Hughbanks, M. Kertesz, P. H. Bird, A hypothetical metallic allotrope of carbon. *J. Am. Chem. Soc.* **105**, 4831–4832 (1983).
10. E. A. Belenkov, V. A. Ali-Pasha, Carbon phases from sp^2 hybridized atoms with three-dimensional rigidly bound structure. *Russ. Phys. J.* **53**, 1280–1285 (1983).
11. H. Bu, M. Zhao, W. Dong, S. Lu, X. Wang, A metallic carbon allotrope with superhardness: A first-principles prediction. *J. Mater. Chem. C* **2**, 2751–2757 (2014).
12. Y. Ma *et al.*, Novel carbon allotropes in all-sp^2 bonding networks: Self-assembling design and first-principles calculations. *Phys. Chem. Chem. Phys.* **25**, 21573 (2023).
13. H. Bu, M. Zhao, A. Wang, X. Wang, First-principles prediction of the transition from graphdiyne to a superlattice of carbon nanotubes and graphene nanoribbons. *Carbon* **65**, 341–348 (2013).
14. Y. Wang *et al.*, Graphdiyne under pressure: A raman study. *Appl. Phys. Lett.* **113**, 021901 (2018).
15. J. Tauc, R. Grigorovici, A. Vancu, Optical properties and electronic structure of amorphous germanium. *Phys. Status Solidi B.* **15**, 627–637 (1966).
16. R. H. Baughman, Solid-state synthesis of large polymer single crystals. *J. Polym. Sci.* **12**, 1511–1535 (1974).
17. N. Narita, S. Nagai, S. Suzuki, K. Nakao, Electronic structure of three-dimensional graphyne. *Phys. Rev. B* **62**, 11146–11151 (2000).
18. A. P. Thompson *et al.*, LAMMPS - a flexible simulation tool for particle-based materials modeling at the atomic, meso, and continuum scales. *Comput. Phys. Commun.* **271**, 108171 (2022).
19. A. C. T. van Duin, S. Dasgupta, F. Lorant, W. A. Goddard, ReaxFF: A reactive force field for hydrocarbons. *J. Phys. Chem. A* **105**, 9396–9409 (2001).
20. R. K. Mohamed, P. W. Peterson, I. V. Alabugin, Concerted reactions that produce diradicals and zwitterions: Electronic, steric, conformational, and kinetic control of cycloaromatization processes. *Chem. Rev.* **113**, 7089–7129 (2013).
21. V. H. Crespi, L. X. Benedict, M. L. Cohen, S. G. Louie, Prediction of a pure-carbon planar covalent metal. *Phys. Rev. B* **53**, R13303–R13305 (1996).
22. H. Terrones *et al.*, New metallic allotropes of planar and tubular carbon. *Phys. Rev. Lett.* **84**, 1716–1719 (2000).
23. A. N. Enyashin, A. L. Ivanovskii, Graphene allotropes. *Phys. Status Solidi B* **248**, 1879–1883 (2011).
24. S. Ma, S. Zhang, L. Z. Sun, K. W. Zhang, High-temperature behavior of monolayer graphyne and graphdiyne. *Carbon* **99**, 547–555 (2016).
25. A. T. Balaban, C. C. Rentia, E. Ciupitu, Chemical graphs. 6. Estimation of relative stability of several planar and tridimensional lattices for elementary carbon. *Rev. Roum. Chim.* **13**, 231–247 (1968).
26. G. Brunetto *et al.*, Nonzero gap two-dimensional carbon allotrope from porous graphene. *J. Phys. Chem. C* **116**, 12810–12813 (2012).
27. N. Diana *et al.*, Carbon materials with high pentagon density. *J. Mater. Sci.* **56**, 2912–2943 (2021).
28. C.-T. Toh *et al.*, Synthesis and properties of free-standing monolayer amorphous carbon. *Nature* **577**, 199–203 (2020).
29. A. Amirav, S. Dagan, A direct sample introduction device for mass spectrometry studies and GC-MS analysis. *Europ. Mass. Spectrom.* **3**, 105–111 (1997).
30. G. Kresse, J. Furthmuller, Efficiency of ab-initio total energy calculations for metals and semiconductors using a plane-wave basis set. *Comp. Mater. Sci.* **6**, 15–50 (1996).
31. J. P. Perdew, K. Burke, M. Ernzerhof, Generalized gradient approximation made simple. *Phys. Rev. Lett.* **77**, 3865–3868 (1996).
32. A. V. Krukau, O. A. Vydrov, A. F. Izmaylov, G. E. Scuseria, Influence of the exchange screening parameter on the performance of screened hybrid functionals. *J. Chem. Phys.* **125**, 224106 (2006).
33. S. Grimme, S. Ehrlich, L. Goerigk, Effect of the damping function in dispersion corrected density functional theory. *J. Comput. Chem.* **32**, 1456-1465 (2011).
34. K. Chenoweth, A. C. van Duin, W. A. Goddard, ReaxFF reactive force field for molecular dynamics simulations of hydrocarbon oxidation. *J. Phys. Chem. A* **112**, 1040–1053 (2008).
35. S. G. Srinivasan, A. C. T. van Duin, P. Ganesh, Development of a ReaxFF potential for carbon condensed phases and its application to the thermal fragmentation of a large fullerene. *J. Phys. Chem. A* **119**, 571–580 (2015).
36. S. Sihn, V. Varshney, A. K. Roy, B. L. Farme, Modeling for predicting strength of carbon nanostructures. *Carbon* **95**, 181–189 (2015).
37. G. B. Kanegae, A. F. Fonseca, Effective acetylene length dependence of the elastic properties of different kinds of graphynes. *Carbon Trends* **7**, 100152 (2022).

PNAS

Supporting Information for

A planar-sheet non-graphitic zero-bandgap sp²-carbon phase made by low-temperature reaction of γ-graphyne

Authors: Ali E. Aliev[1], Yongzhe Guo[2], Alexandre F. Fonseca[3], Joselito M. Razal[4], Zhong Wang[1], Douglas S. Galvão[3], Claire M. Bolding[5], Nathaniel E. Chapman-Wilson[5], Victor G. Desyatkin[5], Johannes E. Leisen[6], Luiz A. Ribeiro Junior[7], Guilherme B. Kanegae[3], Peter Lynch[4,8], Jizhen Zhang[4,8], Mia A. Judicpa[4,8], Aaron M. Parra[1], Mengmeng Zhang[1], Enlai Gao[3], Lifang Hu[9], Valentin O. Rodionov[5]*, Ray H. Baughman[1]*

*Corresponding authors: Valentin O. Rodionov; Ray H. Baughman
Email: vor2@case.edu (V.O.R.); ray.baughman@utdallas.edu (R.H.B)

Affiliations
[1]Alan G. MacDiarmid NanoTech Institute, University of Texas at Dallas, Richardson, TX 75080, USA.
[2.]School of Civil Engineering, Wuhan University, Wuhan, Hubei 430072, China.
[3]Universidade Estadual de Campinas, Instituto de Física Gleb Wataghin, Departamento de Física Aplicada, Campinas, São Paulo 13083-970, Brazil.
[4]Institute for Frontier Materials, Deakin University, Waurn Ponds, Victoria 3216, Australia.
[5]Department of Macromolecular Science and Engineering, Case Western Reserve University, Cleveland, OH 44106, USA.
[6]School of Chemistry and Biochemistry, Georgia Institute of Technology, Atlanta, GA 30332, USA.
[7]Institute of Physics and Computational Materials Laboratory, Institute of Physics, University of Brasília, 70910-900 Brasília, Brazil.
[8]Commonwealth Scientific and Industrial Research Organisation (CSIRO), Waurn Ponds, Victoria 3216, Australia.
[9]Materials Science and Engineering, University of Texas at Dallas, Richardson, TX 75080, USA.

This PDF file includes: Supporting text
                               Figures S1 to S27
                               Tables S1 to S8
                               SI References

1

Contents

1. Nomenclature and Abbreviations

Nomenclature and Abbreviations

Abbreviation	Description
DCM	Dichloromethane
DFT	Density Functional Theory
DMSO	Dimethyl sulfoxide
EI-MS	Electron Ionization Mass Spectrometry
FTIR	Fourier Transform Infrared Spectroscopy
GC-MS	Gas Chromatography–Mass Spectrometry
MD	Molecular Dynamics
MSD	Mass Selective Detector
NMR	Nuclear Magnetic Resonance
Py	Pyridine
TBAF	Tetra-n-butylammonium Fluoride
TBTEB	1,3,5-Tribromo-2,4,6-triethynylbenzene
TEA	Triethylamine
THF	Tetrahydrofuran
TLC	Thin Layer Chromatography
TSP	Thermal Separation Probe
UV-Vis	Ultraviolet-Visible

2. Synthetic Procedures

1,3,5-tribromo-2,4,6-triiodobenzene
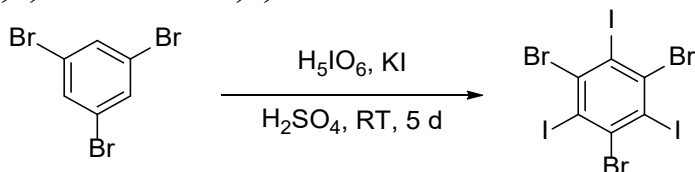
Periodic acid (41.03 g, 180 mmol) was added in small portions over 15 minutes to concentrated H_2SO_4 (500 mL) at room temperature. After dissolution of the periodic acid, crushed KI (89.64 g, 540 mmol) was added in small portions at 0°C over 1 hour. To the resulting deep purple solution at 0°C was added 1,3,5-tribromobenzene (18.89 g, 60.0 mmol) in small portions over 25 minutes. After the solution was stirred at room temperature for 5 days, the resulting thick mixture was poured onto ice. The resulting precipitate was filtered and washed with H_2O (5 × 400 mL) and then MeOH (5 × 400 mL) to give 1,3,5-tribromo-2,4,6-triiodobenzene (42 g) as a light cream-colored solid. The substance was dissolved in hot pyridine (250 mL) and filtered, after which ethanol (750 mL) was added to the resulting solution at room temperature to yield a solid. The solid was filtered and washed with ethanol (3 × 100 mL). The solid was dried under high vacuum for 3 days to give 1,3,5-tribromo-2,4,6-triiodobenzene (30 g, 72%) as a pale-yellow solid. The IR spectroscopy signatures (neat) were v_{max} = 1488, 1354, 1262, 1227, 1147, 1002, 858, 771, 739, 554, 508 cm^{-1}. There was no signal for ^{1}H NMR (500 MHz, DMSO-d6). The ^{13}C NMR (126 MHz in DMSO-d6) provided δ values of 138.61 and 108.23 for the Br substituted carbons and iodine-substituted carbons, respectively. For EI-MS fragmentation, the m/z were 695.5, 693.5, 691.5, 689.5, 567.6, 566.6, 565.6, 564.6, 439.7, and 437.6.

^{13}C-Labeled ((2,4,6-tribromobenzene-1,3,5-triyl)tris(ethyne-2,1-diyl))tris(trimethylsilane)
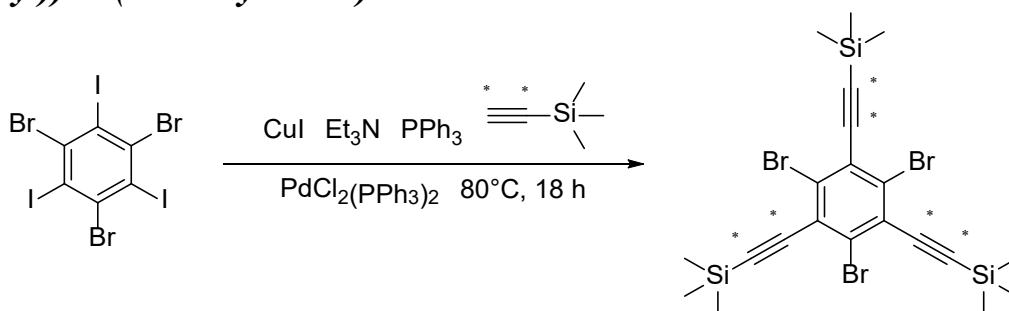
1,3,5-tribromo-2,4,6-triiodobenzene (139 mg, 0.2 mmol), [PdCl$_2$(PPh$_3$)$_2$] (42 mg, 0.06 mmol, 30 mol%), CuI (8 mg, 0.04 mmol, 20 mol%), Et$_3$N (10 mL), and THF (8 mL) were added to a dry three-necked flask. The flask was sealed and the contents were degassed by three freeze-pump thaw cycles. Trimethylsilylacetylene-^{13}C$_2$ (300 mg, 3 mmol) and Ph$_3$P (21 mg, 0.08 mmol, 40 mol%) were added to the mixture. The mixture was stirred at 80°C for 18 h under argon. After the removal of solvent in a rotary evaporator, the residue was further purified by flash chromatography using n-hexane as the eluent to yield labeled ((2,4,6-tribromobenzene-1,3,5-triyl)tris(ethyne-2,1-

diyl))tris(trimethylsilane) as a white solid (25 mg, 0.041 mmol, yield: 21%). IR spectroscopy signature (neat) v_{max} = 2958, 2924, 2853, 2085, 1338, 1251, 1005, 844, 760, 704, 632 cm⁻¹. ¹H NMR (500 MHz, CDCl₃) δ 0.29 (d, J_{CH} = 2.8 Hz, 27H, Si(CH₃)₃). ¹³C NMR (126 MHz, CDCl₃) δ 129.17 (d, J = 18.7 Hz, CBr), 127.44 (dd, J = 95.5, 9.9 Hz, C_6C≡C), 107.00 (dd, J = 141.9, 45.7 Hz, ¹³C-enriched C≡CSi), 101.66 (dd, J = 141.8, 20.0 Hz, ¹³C-enriched C_6C≡C), -0.23 (d, J = 5.3 Hz, Si(CH₃)₃).

The substance contains a 2% impurity (determined by ¹H NMR) of 1,4-bis(trimethylsilyl)buta-1,3-diyne. ¹H NMR (500 MHz, CDCl₃) δ 81.72 (d, J = 13.8 Hz), 80.24 (d, J = 14.4 Hz). ¹³C NMR (126 MHz, CDCl₃) δ 87.90 (dd, J = 185.6, 33.1 Hz, ¹³C-enriched C≡CSi), 80.98 (dd, J = 185.6, 14.1 Hz, ¹³C-enriched C≡CSi), the signal from Si(CH₃)₃) is invisible.

¹³C-Labeled TBTEB
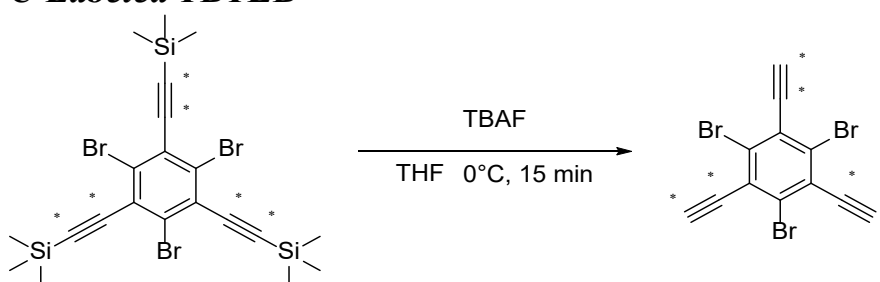
To a solution of labeled ((2,4,6-tribromobenzene-1,3,5-triyl)tris(ethyne-2,1-diyl))tris (trimethyl-silane) (25 mg, 0.041 mmol) in THF (5 mL) was added 90 µL TBAF (75% solution in water, 0.247 mmol) and stirred at 0°C for 15 minutes. The solution was then diluted with ethyl acetate, washed with distilled water, and dried with anhydrous Na₂SO₄. The solvent was removed on a rotary evaporator. The residue was further purified by flash chromatography using hexanes as the eluent to give labeled 1,3,5-tribromo-2,4,6-triethynylbenzene (TBTEB) as a white solid (11 mg, 0.028 mmol, yield: 67%). 4-bis(trimethylsilyl)buta-1,3-diyne was converted to buta-1,3-diyne during the reaction, which subsequently evaporated. IR spectroscopy signature (neat) v_{max} = 3261, 2931, 2864, 2043, 1519, 1334, 960, 736, 678, 634 cm⁻¹. ¹H NMR (500 MHz, CDCl₃) δ 3.76 (dd, J = 254.3, 52.7 Hz, 3H, C≡CH). ¹³C NMR (126 MHz, CDCl₃) δ 130.29 (CBr), 127.35 (dd, J = 102.5, 13.8 Hz, C_6C≡CH), 88.29 (d, J = 185.7 Hz, ¹³C-enriched C≡CH), 80.81 (d, J = 185.7 Hz, ¹³C-enriched C_6C≡CH).

¹³C-Labeled Graphyne

Labeled TBTEB (11 mg, 0.028 mmol), Pd(PPh₃)₄ (33 mg, 0.028 mmol), and CuI (0.4 mg, 0.002 mmol) were placed in a Schlenk flask under argon atmosphere and pyridine (5 mL) was added. The tube was sealed and the contents were degassed by three freeze-pump-thaw cycles. The reaction mixture was stirred under an argon atmosphere at 110°C for 3 days, and then *N,N*-diethyl-2-phenyldiazene-1-carbothioamide (100 mg) was added and the reaction mixture was stirred for 2 hours at room temperature. The reaction mixture was concentrated by a rotary evaporator. The solid product was washed with toluene, ethyl acetate, water, isopropanol, ethanol, methanol, and acetone (each 40 mL) on the filter (a 0.2 µm, TF-200 (PTFE) membrane). Then the residue was dried under a high vacuum for 3 days to give the black solid (7.6 mg).

3. Experimental Structural Characterization of Precursors

^{1}H NMR, ^{13}C NMR, FTIR, and TSP-EI-MS spectra relevant for the synthesis and structure of ^{13}C-labeled graphyne are in *SI Appendix*, Figs. S1 and S3, *SI Appendix*, Figs. S2 and S4-S9, *SI Appendix*, Figs. S6 and S7, and *SI Appendix*, Figs. S10-S14, respectively.

4. Impurities measured by energy-dispersive X-ray spectroscopy for the presently used graphyne

The structure and properties of the presently investigated graphyne do not significantly differ from those we initially reported for graphyne, which is expected since the originally reported synthesis method was used for the present graphyne. For example, the synchrotron-measured diffraction spacings were the same for these samples within the experimental error, when these spacings were measured for graphyne that was in a rotating capillary tube. However, since we did not previously characterize the element content by energy-dispersive X-ray spectroscopy (EDX), we here provide these new results, which are likely more reliable than the previously reported element analysis by X-ray photoelectron spectroscopy (XPS), which are most sensitive to impurities close to the sample surface, because of surface absorption effects.

EDX spectroscopy results for the as-synthesized graphyne powder indicates that it is 66.4 wt% carbon and the previously reported XPS measurements indicate that there is a 1:1 ratio of sp to sp^2 carbons in the graphyne powder (7), which is consistent with γ-graphyne. The average palladium content from EDX spectroscopy does not exceed 1 at% for multiple samples. There is no evidence of silver or gold from the silver paste or gold-coated silicon wafer on which the graphyne powder is mounted. Most likely, the penetration depth of scattered electrons does not exceed the thickness of graphyne particles (~ 20-50 µm). The observed oxygen may be physically absorbed rather than chemisorbed and varies between samples.

5. Experimental Characterization of the Structural Transformation and Other Effects of Thermal Annealing

Raman spectra during the structural transition

The synchrotron diffraction peaks of the presently investigated graphyne agree with those observed for the identically synthesized graphyne used for our previous work (7) and are consistent with the theoretically predicted graphyne structures and with previous electron diffraction determined diffraction spacings (7) for (h,k,0) reflections (*SI Appendix,* Table S1). The Raman spectra were collected on a DXR3 Raman Microscope (Thermo-Fisher Scientific Inc.) using a laser excitation wavelength of 532 nm. To avoid exposure of the graphyne sample to oxygen at high temperatures, we used step-by-step annealing in a high vacuum station (0.1 mTorr) to progressively increased temperatures for one hour at each temperature. After each thermal annealing step, the Raman spectrum was collected at room temperature (T_{RT}) using as low as possible laser beam power to avoid overheating of the investigated low-density graphyne particle (which was typically ~200x200x50 μm^3). For the chosen lens magnification of X10 and a 50 μm pinhole aperture, the spectra were collected using a laser beam power of 0.2 mW and a scan time of 5 s for 64 collection scans.

$SI\ Appendix$, Fig. S16 compares the TGA thermogravimetric mass loss measurements and the DSC heat flow measurements for graphyne, which indicates that much of the calorimetrically-measured exotherm is over before major mass loss occurs by volatilization.

$SI\ Appendix$, Fig. S17 shows the Raman spectra of a graphyne sample that was heated consecutively to 100, 150, 175, 200, 240, 260, 280, 300, and 320ºC for 1 hour and measured at room temperature. As the narrow triple bond transition at 2193 cm^{-1} disappears during heating, wide G and D peaks were present that are specific for highly oriented pyrolytic graphite (HOPG) and for carbon structures containing aromatic rings. In a highly crystalline structure of HOPG, here used for wavelength calibration, the optical in-plane stretching vibrations of neighboring carbons (E2g) are concentrated at 1582 cm^{-1}. In the graphyne studied here, the G-band of the pristine sample is shifted to lower frequencies than for HOPG, ~1545 cm^{-1}. However, heat treatment above the peak of the exothermic reaction temperature (~250ºC) shifts the G-band to higher wavenumbers, ~1582 cm^{-1} for samples heated to 350ºC and ~1595 cm^{-1} for a sample heated up to 500ºC. The position of triple-bond carbon vibration is independent of the thermal treatment, but the intensity of the peak strongly decays above 175ºC (*SI Appendix*, Fig. S17B). *SI Appendix*, Fig. S18 shows the room-temperature FT-IR absorbance plots for a progressively thermally annealed graphyne sample that was exploited for the Tauc absorption plot of Fig. 1D, which yielded the spectroscopic average bandgap plot in the bottom panel of Fig. 1.

The intensity of the G-band peak in *SI Appendix*, Fig. S17B increases by a factor of about three as the annealing temperature increases from the start of the phase transition exotherm to its peak and then decreases to slightly below the pretransition level, while the triple-bond vibration intensity continuously decreases to near zero. This increase in aromatic vibration intensity with decreasing a triple-bond Raman intensity is consistent with our proposed elimination of triple-

bonds by in-plane reaction to form new aromatic rings. However, this behavior of the G-band peak is difficult to fully analyze, since the depth of the penetration of the laser excitation beam will decrease as the transitioning graphyne becomes more absorbing because of the decrease in its bandgap that is shown in the bottom plots of Fig. 1.

Observing the transformation of ^{13}C labeled triple bonds in graphyne to exclusively sp^2 carbons by NMR spectroscopy

NMR spectroscopy is a natural choice for investigating structural changes that impact hybridization or interatomic distances. However, initial ^{13}C solid-state NMR experiments on as-synthesized graphyne revealed that the T_1 spin-lattice relaxation time for the core carbons is exceptionally long, consistent with observations in graphitic carbon nanostructures (1, 2). As a result, the sensitivity of the experiments was low, and the obtained spectra were less informative than anticipated.

To address this limitation, we synthesized graphyne selectively labeled with ^{13}C on all acetylenic bonds (*SI Appendix*, Figs. S1-S7). After labeling these bonds in the precursor monomer with ^{13}C, graphyne was made from the labeled graphyne precursor (TMS-acetylene-^{13}C$_2$) using our previously described method (7). A ^{13}C DP-MAS solid-state NMR spectrum of this labeled graphyne was then acquired (*SI Appendix*, Fig. S8). This spectrum shows two peaks consistent with acetylenic carbons centered at ~90 and 83 ppm. Based on the routine ^{13}C spectrum of the TBTEB precursor (*SI Appendix*, Fig. S5), the peak at 90 ppm can be assigned to the terminal alkynes, and the peak at 83 ppm to the internal alkynes.

Although the apparent population of internal alkynes in this experiment appears larger than the population of terminal alkynes, the ratio between these species requires further investigation. The T_1 spin-lattice relaxation times for crystalline samples can be very long. Thus, even with a long scan delay, detecting certain slow-relaxing populations of spins can be challenging. We used a 180 s pulse delay following the protocol previously used for DP-MAS of ^{13}C-labeled graphene oxide (2). However, the crystallinity of our graphyne samples is higher than that of typical graphene oxide. Therefore, it is highly likely that the population of the slower relaxing internal alkynes is underestimated in this experiment. Only the ^{13}C-labeled carbons are detected here. The simple structure of the alkyne region and lack of other prominent NMR peaks indicate that, under our typical conditions of graphyne synthesis, the acetylenic carbons do not undergo significant side reactions (such as spontaneous Masamune-Bergman aromatization).

The sample of selectively labeled graphyne was then heated from ambient temperature to 325°C. The heating program had a single 2°C/min ramp from 100°C to the final temperature, consistent with prior DSC experiments. The DP-MAS ^{13}C solid-state NMR spectrum of the sample after this thermal anneal revealed the complete disappearance of the acetylenic carbons (*SI Appendix*, Fig. S9). The spectrum indicates that these carbons have been transformed into a single type of sp^2 species with a chemical shift of ~130 ppm, most consistent with aromatic carbons. Additionally, a significant decrease in the T_1 relaxation time was observed. This implies that either the material's surface became more accessible to ambient oxygen, the material's crystallinity decreased, or both factors were at play.

A cross-polarization (CP-MAS) NMR experiment indicated no signal enhancement in comparison with the DP-MAS experiment, which means the new sp^2 carbons are not co-localized with any protons. This suggests that the transformation of graphyne did not involve abstraction of adventitious hydrides in the same way as previously described for a small-molecule model (3).

Solid-state NMR of ^{13}C-labeled graphyne (Section 2 and *SI Appendix*, Fig. S8) was conducted using a Bruker Avance I operating at a ^{1}H frequency of 800 MHz. ^{13}C spectra were recorded using a direct polarization (DP) sequence with ^{1}H decoupling and a repetition delay of 180 seconds under conditions of magic angle spinning at room temperature. The spinning speed was 40 kHz, using a narrow-bore Bruker H/C/N Triple Resonance CPMAS probe operating with 1.3 mm outer diameter rotors. A representative spectrum was recorded using a total of 400 scans.

Solid-state NMR of the thermally treated sample of ^{13}C-labeled graphyne (heated to 325ºC, *SI Appendix*, Fig. S9) was conducted using a Bruker AV3-500 operating at a ^{1}H frequency of 500 MHz. ^{13}C spectra were recorded using a direct polarization sequence with ^{1}H decoupling and a repetition delay of 5 seconds under conditions of magic angle spinning at room temperature. The spinning speed was 20 kHz, using a narrow-bore Bruker HX-MAS probe operating with 3.2 mm outer diameter rotors. A representative spectrum was recorded using a total of 10240 scans. The intensity of spectra with repetition delays ranging from 0.5 seconds to 500 seconds was used to calculate the ^{13}C T_1 relaxation times from the buildup of signal intensities with increasing repetition delays.

Unusual kinetic aspects of the structural transformation of graphyne

Heat flow measurements were conducted using the temperature-modulated mode of the TA differential scanning calorimeter (DSC) TA Q-2000. The heating rate was 2ºC/min. The chamber was continuously purged by nitrogen gas. To avoid the chemical interaction of vapor with the graphyne, an ~10 μm diameter hole was punctured in the top lid of the aluminum sample pan.

Unexpected behavior was observed for a graphyne sample heated to a low temperature (150°C) in the exothermic reaction range, annealed at this temperature for one hour, and then cooled down to 40°C before this process was conducted at the same heating rate (2°C/min) to a 25°C higher temperature (*SI Appendix*, Fig. S22). No exotherm occurred during reheating until the annealing temperature was reached or nearly reached and then it briefly occurred and then stopped when the temperature scan was ended because the next higher annealing temperature was reached. This behavior suggests that regions of the reacting graphyne, at the obtained degrees of conversion, transform when their local free energy change reaches essentially zero. *SI Appendix*, Fig. S22 shows the close correlation between these results and the heat flow resulting from heating the graphyne at an uninterrupted heating rate of 2ºC/min.

6. Electrochemical Measurements for Graphyne Annealed One Hour at Progressively Higher Temperatures

This section provides additional information for the electrochemical CV measurements described in the text and in *SI Appendix*, Figs. S20 and S21. These measurements were conducted on a 5-layer stack of forest-drawn multiwall carbon nanotube (MWNT) sheets that were spray-coated layer-by-layer with graphyne from a dispersion of graphyne in dimethylformamide. Electrochemical CV measurements were conducted in 0.1 M tetrabutylammonium hexafluorophosphate in acetonitrile and a high-surface-area Pt counter electrode and an Ag/Ag^+ reference electrode were deployed. These measurements were made for an electrode potential between -1 to 1.5 V vs Ag/Ag^+ and a 50 mV/s scan rate. Separate CV experiments were conducted on a non-annealed MWNT stack and a graphyne/MWNT layer sheet stack containing about 75 wt% of graphyne and about 25 wt% of MWNT.

The pure MWNT sheet stack had no redox peaks and a CV capacitance of 22 F/g. The non-annealed graphyne/MWNT layer sheet stack had a capacitance of 12.2 F/g. Even though ~3% weight loss occurs on heating graphyne to above 305ºC (*SI Appendix*, Fig. S16), which was not measured for the graphyne/MWNT sheet stack and accounted for in calculating its gravimetric room temperature CV capacitance, the fully non-Faradaic CV-measured capacitance at room temperature after thermal annealing up to 350ºC was 36 F per gram of non-annealed weight. This is very high compared to the CV capacitances of 12.2 F/g and 22 F/g for the non-annealed graphyne/MWNT sheet stack and the non-annealed pure MWNT sheet stack, respectively. Our future work will explore this capacitance advantage of thermally annealed MWNT/graphyne composites by determining the potential scan rate dependence of performance and other key electrochemical aspects.

7. MD and DFT Calculation Results

MD and DFT results for formation energies, density, and other properties are presented for pristine graphyne, stacks of pristine graphyne, polyeneized graphyne, ringized graphyne, and stacked sheets of ringized graphyne. Results are also provided for other novel carbons, like biphenylene (4), which is a possible precursor to graphyne (rather than a possible room-pressure reaction product), because of its higher predicted formation enthalpy than graphyne. The calculated space groups, unit cell parameters, and atomic coordinates of the inter-plane-reacted graphyne structures shown in Fig. 3, labeled by the letters given in this figure, are in *SI Appendix*, Table S6. This same information for the in-plane-reacted ringene structures shown in Fig. 4 is in *SI Appendix*, Table S7.

Graphyne and 3D polyeneized graphyne
As described in the main text, graphyne is theoretically predicted to possibly topochemically react by the inter-sheet reaction of the acetylene groups in graphyne to produce polyacetylene chains. Of the periodic sheet stacking modes illustrated in *SI Appendix*, Fig. S22 (AA, AB1, AB2, and ABC), only the highest energy fully eclipsed AA structure could potentially enable the complete reaction of all triple bonds to form extended polyene chains.

According to Ducéré, Lepetit, and Chauvin (5), the AB1 and ABC configurations are the most stable stackings of graphyne. Of these two sheet stackings, only the AB1 configuration would enable topochemical polymerization to form polyacetylene chains. Moreover, this polymerization would be possible for only 2/3 of the triple bonds, since the other triple bonds in a periodic sheet stack are between phenyl rings in the graphyne. More recent work, such as that by Yun *et al.* (6) and Desyatkin *et al.* (7), found that AB2 is the lowest energy stacking configuration of graphyne. This stacking mode would not allow topochemical polymerization of any acetylene groups. Our present DFT calculations (*SI Appendix*, Table S3) predict that the packing energy at 0 K becomes increasingly favorable in the order AA, AB1, AB2, and ABC, although the energy differences between these stackings of graphyne sheets are small.

The only inter-sheet reacted polyeneized structures considered in this study are those that can be topochemically formed by inter-sheet reactions of acetylene groups of graphyne sheets that have either AA or AB1 stacking configurations, since they are the only considered configurations that can result in the topochemical formation of polyene chains without bond breaking in the graphyne. They are the structures called 2-cis, 1-sp polygraphyne; 2-trans, 1-sp polygraphyne; 3-cis polygraphyne; 1-cis, 2-trans polygraphyne; and 3-trans polygraphyne (see Fig. 3). *SI Appendix*, Table S4 provides the density, formation energies, and percentage shrinkage with respect to non-reacted graphyne. Also, our predicted properties of the Hex-C24 phase previously proposed for reacted graphyne (8) are shown in this table, which has sp^3 carbon atoms formed by inter-sheet reaction of phenyl ring carbons in graphyne sheets as well as trans-polyacetylene chains. For the reacted eclipsed graphyne phase, the 1-cis, 2-trans polygraphyne has a similar DFT-calculated enthalpy change on polymerization (-1.163 kJ/g) as the 3-trans polygraphyne (-1.275 kJ/g). However, while further reaction of 3-trans polygraphyne by coupling the phenyl rings by

sp³ carbon formation is predicted during MD calculations, but not by the likely more reliable DFT calculations, neither calculation predicts this for the other Fig. 3 phases. Importantly, our experimental data indicates that the aromatic rings do not convert to sp³ rings during graphyne thermal reaction at ambient pressure.

Among the structures with only sp and sp² carbon atoms, the 3-trans polygraphyne is the one with the lowest energy by both calculation methods. The structures and their formation energies calculated by ReaxFF agree with DFT calculations in the order of the energy differences between the different polyeneized carbon and that of the non-bonded AB2 graphyne.

2D ringized structures

As described in the main text, we have also investigated topochemical routes for in-plane reactions of graphyne's sp-sp² carbon atoms to produce purely sp² 2D ringized phases. Intra-sheet reaction is predicted to occur via Bergman-like reactions (9, 10), without bond breaking in graphyne, to provide a lower energy structure than graphyne. Other than for the previously investigated biphenylene (4) in *SI Appendix*, Fig. S23 and Table S5, all four of these investigated structures (Fig. 4 and *SI Appendix*, Table S5) that could be formed without bond breaking in graphyne have a lower calculated formation energy than graphyne. Their structures and formation energies that we calculated by ReaxFF agree with our DFT calculations. While other graphene sheet allotropes have been described, such as those of Enyashin and Ivanovskii (11), these structures have either a higher formation energy than graphyne or cannot be formed from graphyne without bond breaking in graphyne. The structure of *SI Appendix*, Fig. S26 is both ringized by in-plane reaction and polyeneized by inter-plane reaction to eliminate all sp bonds.

Calculation of the temperature-dependent heat capacities of graphyne and 5.6.9 ringene and their use for obtaining the temperature dependence of the enthalpy difference between 5,6,9 ringene and graphyne

As discussed in the main text, the lowest energy ringene phase (5,6,9 ringene) is the only candidate product of graphyne reaction that satisfies all of the experimental observations. Consequently, it is especially important to calculate the heat capacity of this phase and that of the parent graphyne, so that the temperature dependence of the enthalpy difference between 5,6,9 ringene and graphyne can be calculated (from 0 K theoretical enthalpies) for all temperatures at which both graphyne and 5,6,9 ringene are thermally stable.

The heat capacities of non-reacted pristine graphyne in the AB2 stacking configuration (*SI Appendix*, Fig. S27) and 5,6,9 ringene having eclipsed sheets were calculated using the Quantum Espresso (QE) code (12, 13), which performs DFT calculations by employing the plane-wave basis-set and pseudopotentials method. The interactions between electrons and the atomic cores are described by an expansion of the wave function by using plane-wave and norm-conserving pseudopotentials. Norm-conserving pseudopotentials generated using the Troullier-Martins method in conjunction with the Perdew-Burke-Ernzerhof (PBE) functional were used to address both exchange energies and electronic exchange-correlation effects (14, 15, 16). To optimize the crystal structure of our model sheets, the Broyden Fletcher Goldfarb Shanno (BFGS) scheme was used as implemented in QE code (17). We set large cutoff values of 70 Ry and 700 Ry for wave-

functions and charge density, respectively. For electronic self-consistency, a convergence criterion of 1.0×10^{-5} eV was employed. During lattice relaxation, the force acting on each atom was kept below 1.0×10^{-3} eV/Å. The optimization process involved a periodic box (representing a bulk system) with a 10×10×10 k-point grid, while electronic property calculations employed a k-point grid of 20×20×20.

Constant-volume heat capacities of periodically stacked sheets of pristine graphyne (in the AB2 stacking configuration of *SI Appendix*, Fig. S22) and eclipsed sheet 5,6,9 ringene (shown in *SI Appendix*, Fig. S27A) were calculated as a function of temperature using the Phonopy package (18) in conjunction with the QE code. Phonopy calculates the phonon spectrum of the investigated material and provides its lattice thermal properties from accurately calculated QE force constants. The second- and third-order interatomic force constants were computed using the supercell finite-displacement approach with step sizes of 1.0×10^{-2} Å. Supercells of 48 atoms (2 sheets) were used to calculate the second-order interatomic force constants. Phonopy provides the temperature-dependent heat capacities of the *SI Appendix*, Fig. S27A structure, where it must be remembered that they are valid only below temperatures where the graphyne transforms and the higher temperatures where the 5,6,9 ringene degrades. *SI Appendix*, Fig. S27B shows that the heat-capacity-based change of the enthalpy of transition is small over relevant temperatures, since the heat capacity difference between the two phases is low when integrated over experimentally relevant temperatures where the graphyne does not transform.
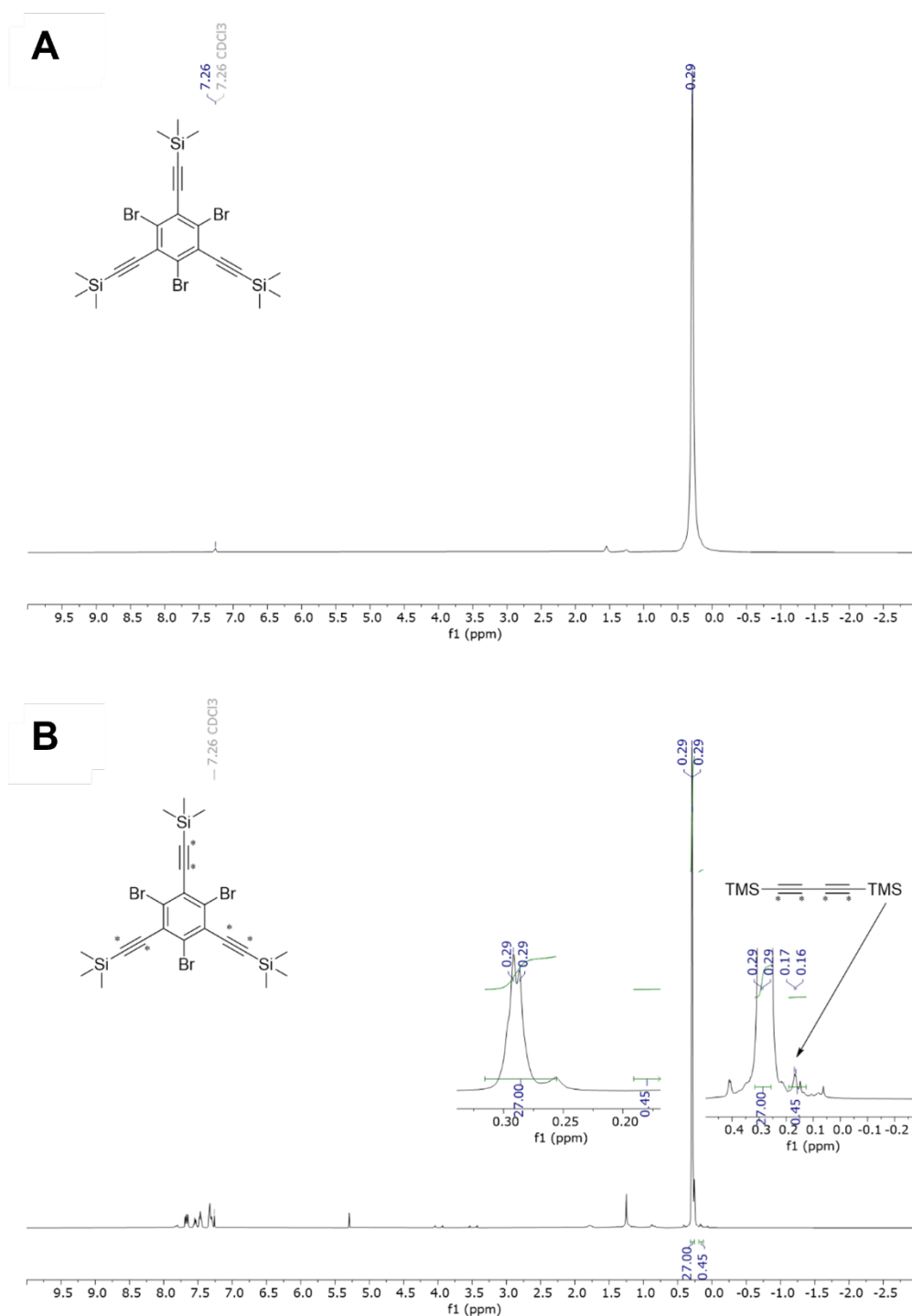
Figures and Tables

Fig. S1. ^{1}H NMR spectrum of unlabeled (*A*) and labeled (*B*) (2,4,6-tribromobenzene-1,3,5-triyl)tris(ethyne-2,1-diyl))tris(trimethylsilane) in CDCl₃. The substance contains a 2% impurity (determined by ^{1}H NMR) of 1,4-bis(trimethylsilyl)buta-1,3-diyne.
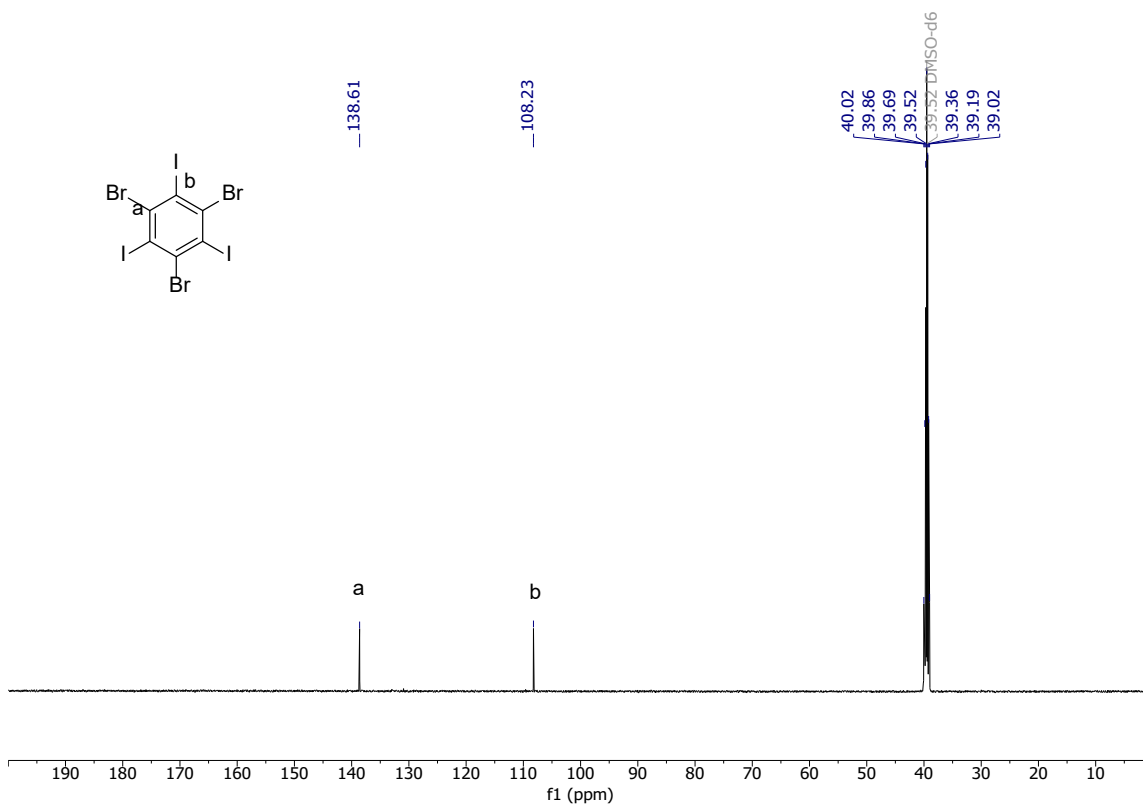
Fig. S2. ^{13}C NMR spectrum of 1,3,5-tribromo-2,4,6-triiodobenzene in DMSO-d6.

Fig. S3. ^{1}H NMR spectrum of unlabeled (*A*) and labeled (*B*) TBTEB in CDCl$_3$.
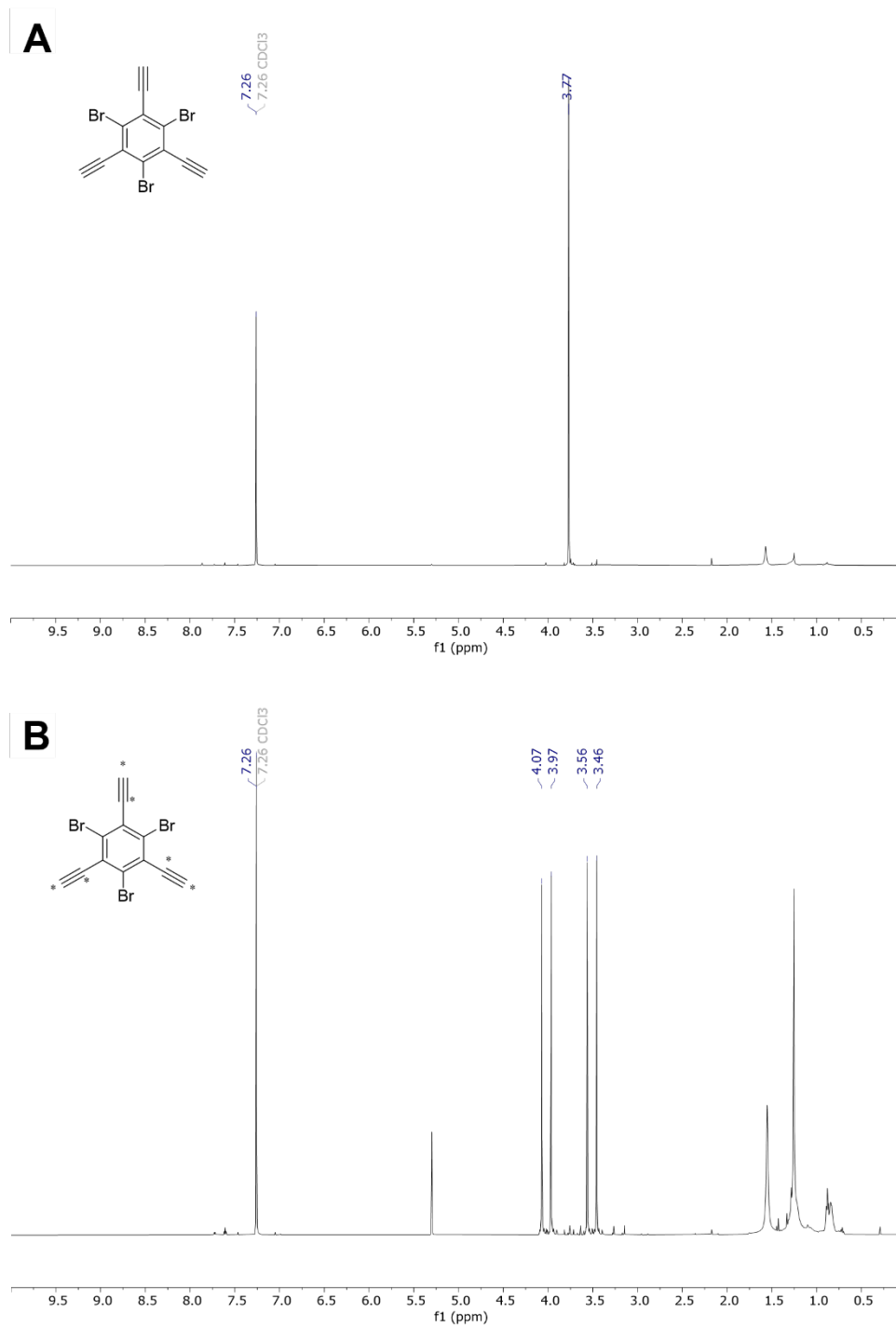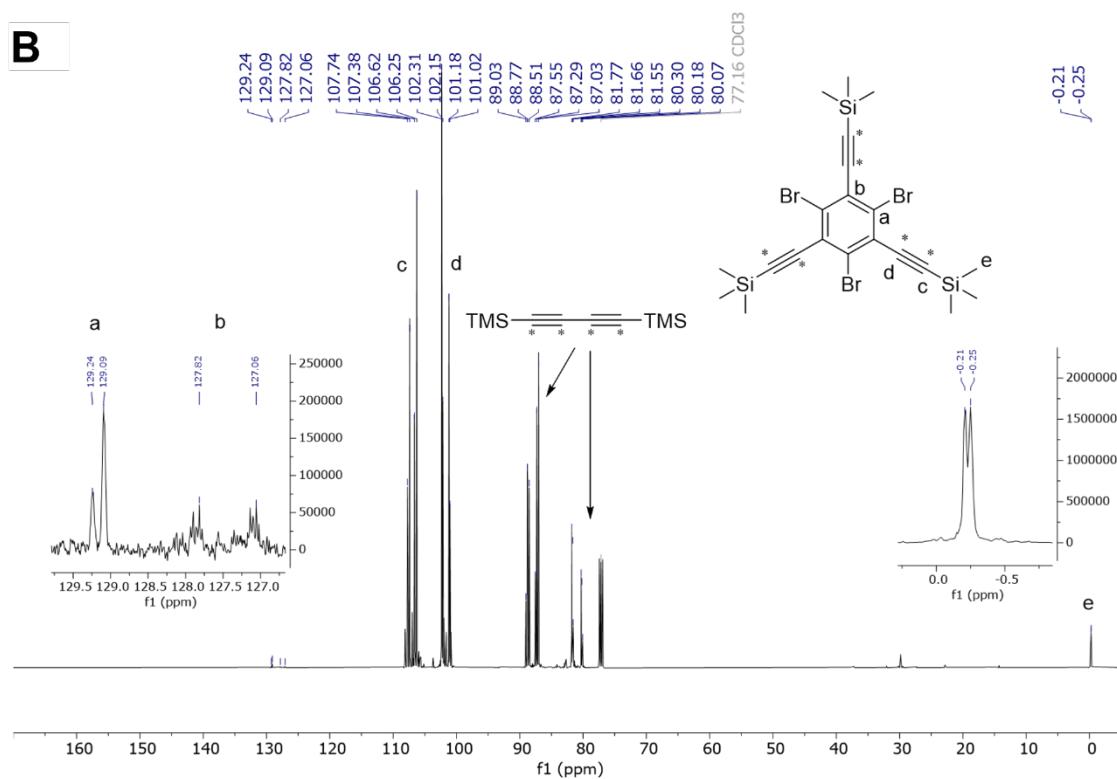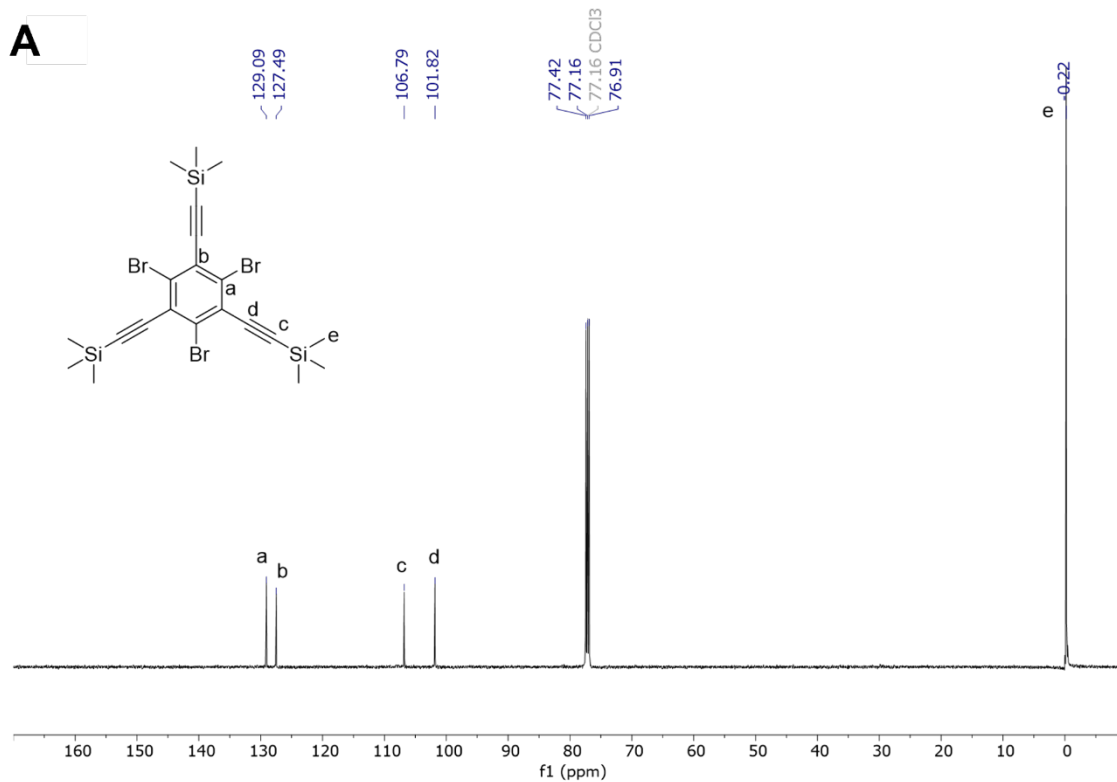
Fig. S4. The ^{13}C NMR spectrum of unlabeled (*A*) and labeled (*B*) ((2,4,6-tribromobenzene-1,3,5-triyl)tris(ethyne-2,1-diyl))tris(trimethylsilane) in CDCl$_3$. (*B*) contains a 2% impurity, which was determined by ^{1}H NMR to be 1,4-bis(trimethylsilyl)buta-1,3-diyne.
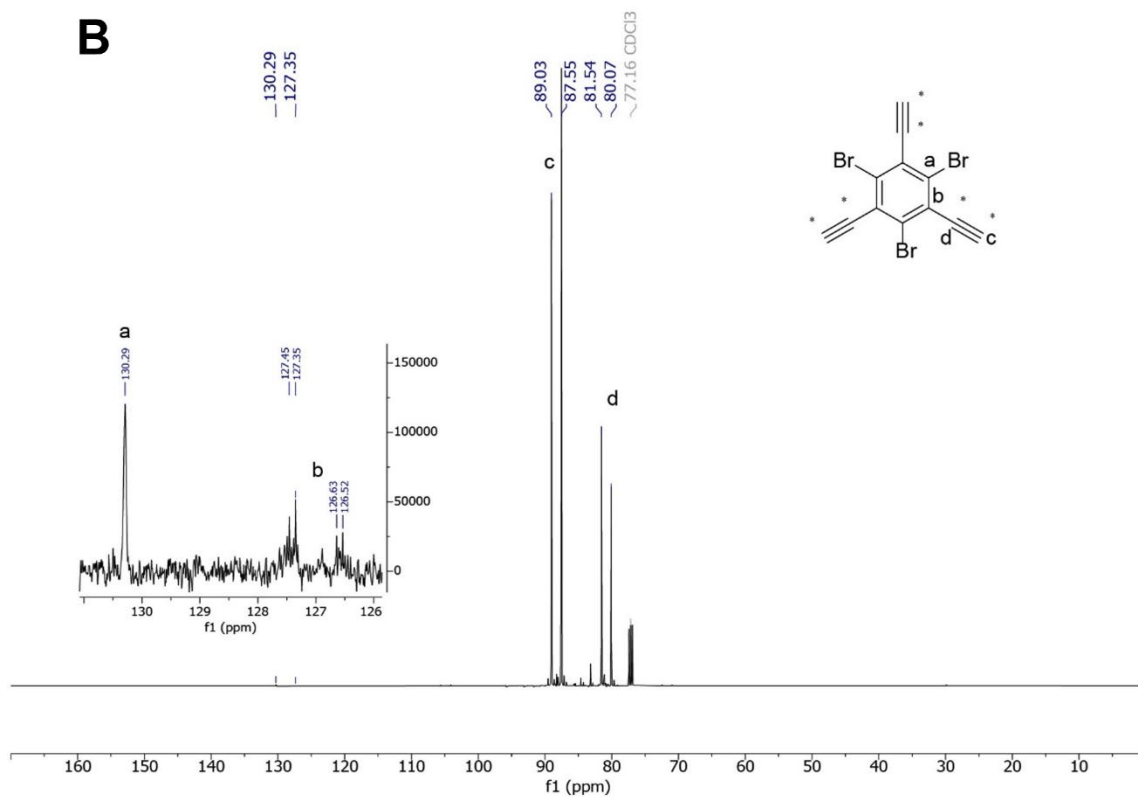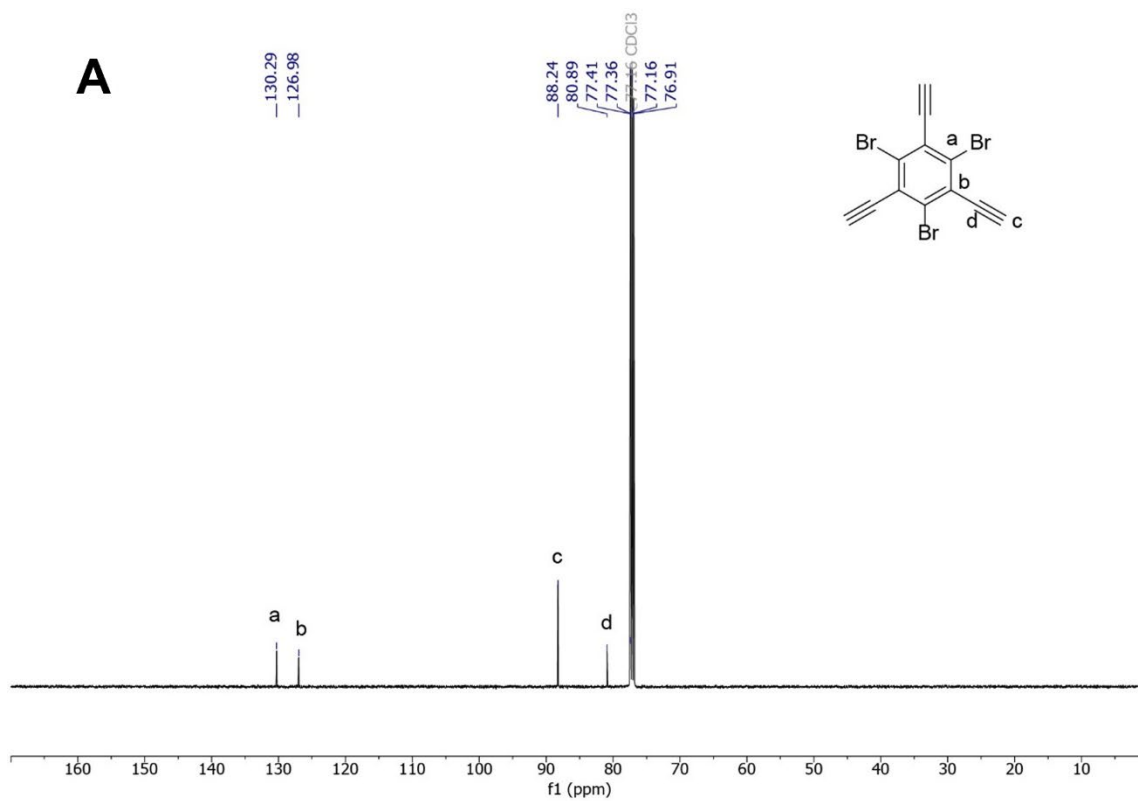
Fig. S5. The ^{13}C NMR spectrum of unlabeled (*A*) and labeled (*B*) TBTEB in CDCl$_3$.
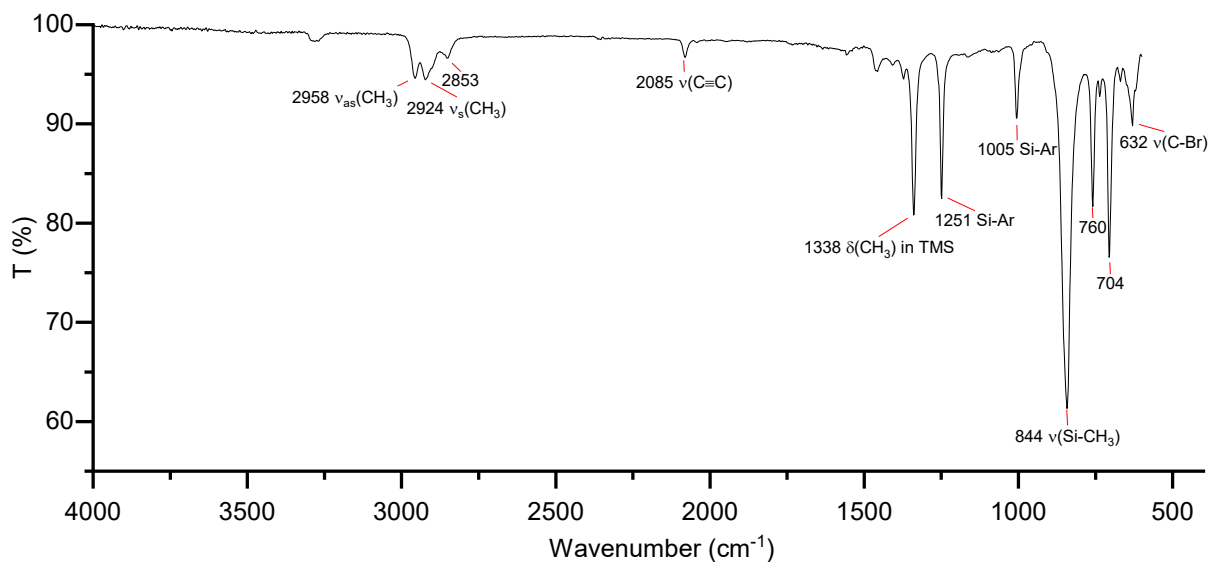
Fig. S6. The FTIR spectrum of ^{13}C labeled (2,4,6-tribromobenzene-1,3,5-triyl)tris(ethyne-2,1-diyl))tris(trimethylsilane).
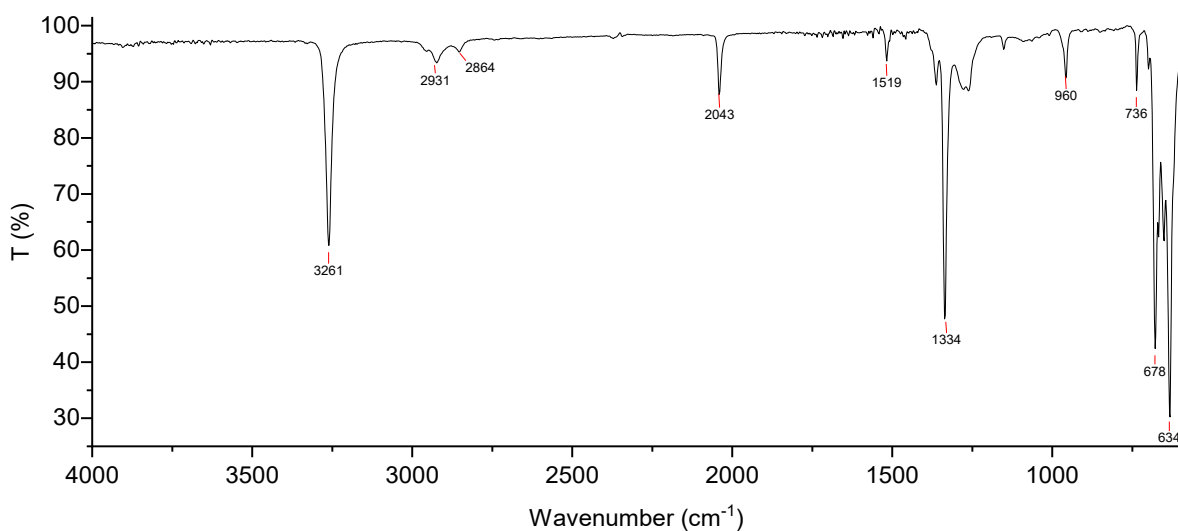
Fig. S7. The FTIR spectrum of labeled TBTEB.

DP ^{13}C solid state MAS
D1 = 180s
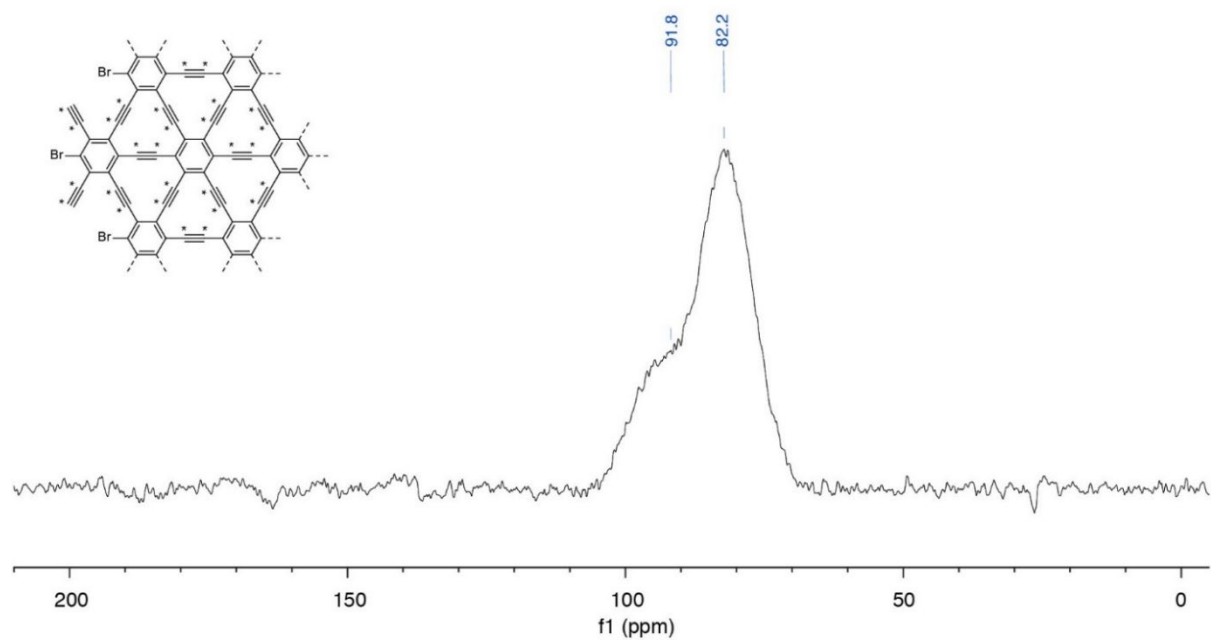
Fig. S8. Room temperature Direct Polarization Magic-Angle Spinning (DP-MAS) ^{13}C solid-state NMR spectrum of γ-graphyne selectively labeled with ^{13}C.
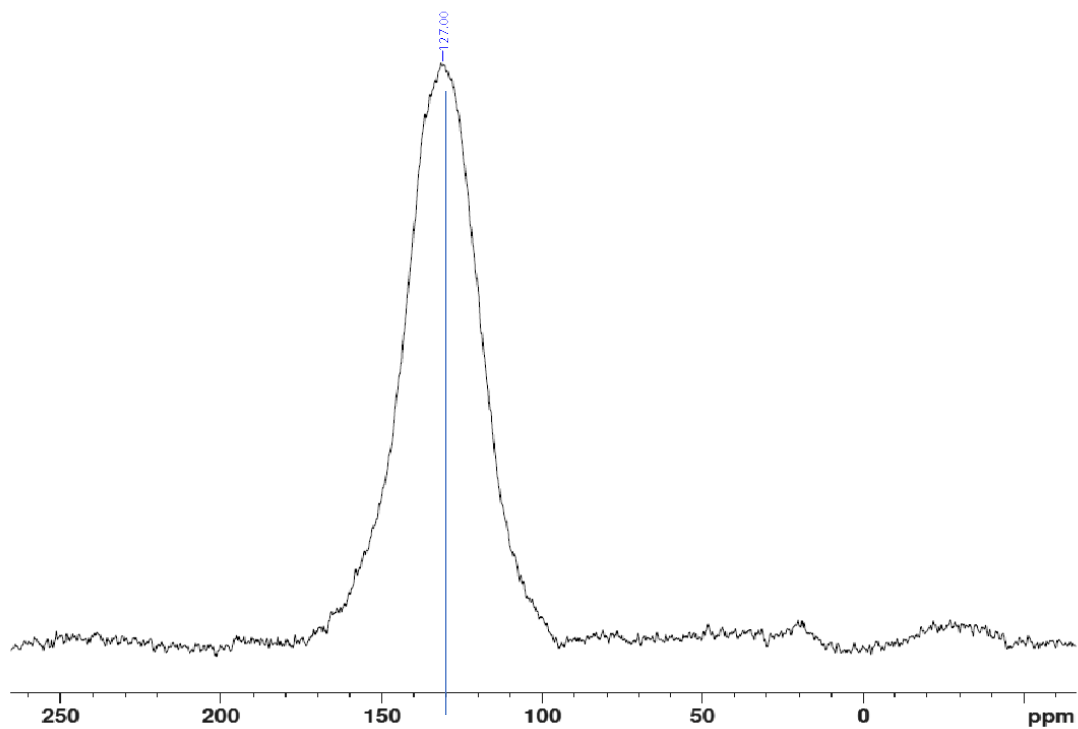
Fig. S9. Room temperature Direct Polarization Magic-Angle Spinning (DP-MAS) ^{13}C solid-state NMR spectrum of the selectively labeled ^{13}C graphyne after thermal annealing by heating from 100ºC to 325ºC at 2ºC/min.
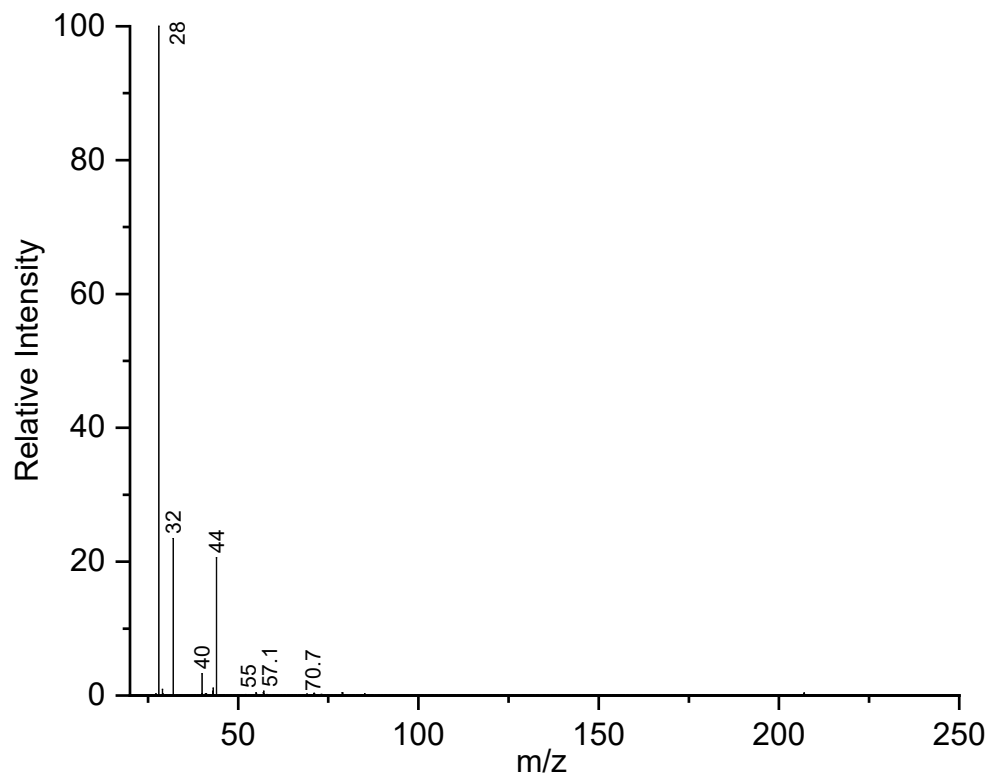
Fig. S10. Electron ionization mass spectrum of Br-edge graphyne volatiles at 150°C.
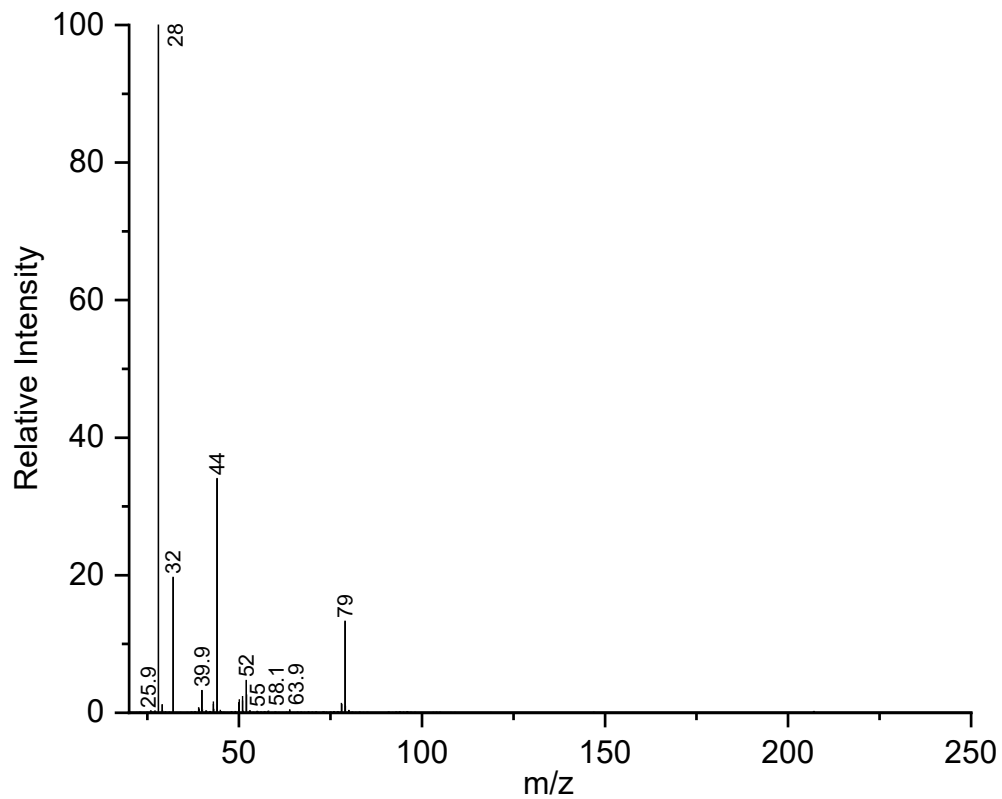
Fig. S11. Electron ionization mass spectrum of Br-edge graphyne volatiles at 210°C.
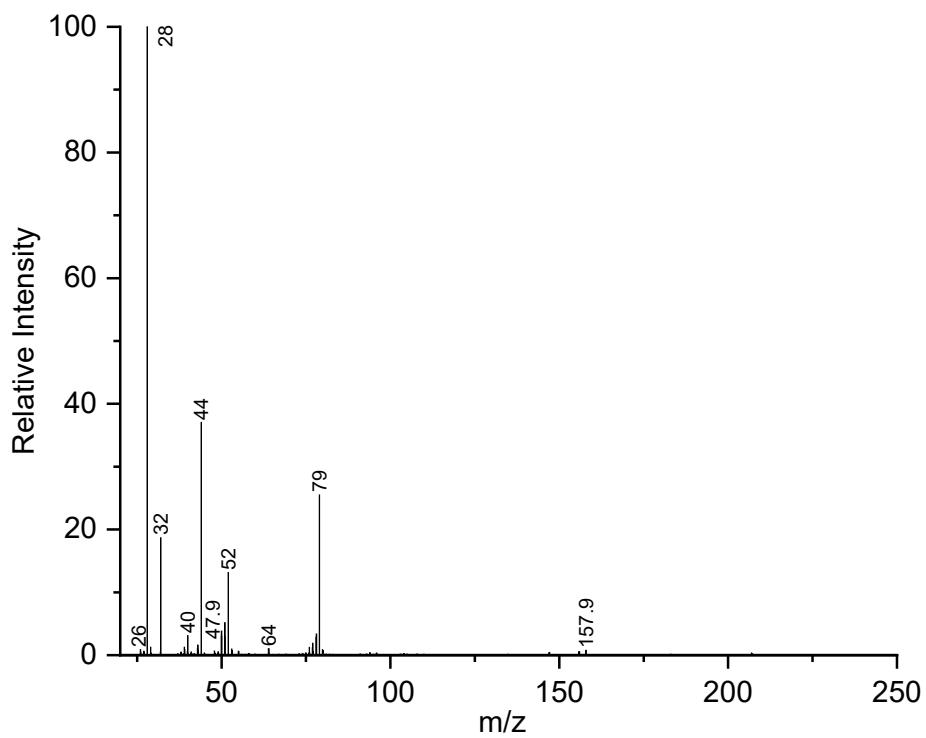
Fig. S12. Electron ionization mass spectrum of Br-edge graphyne volatiles at 250°C.
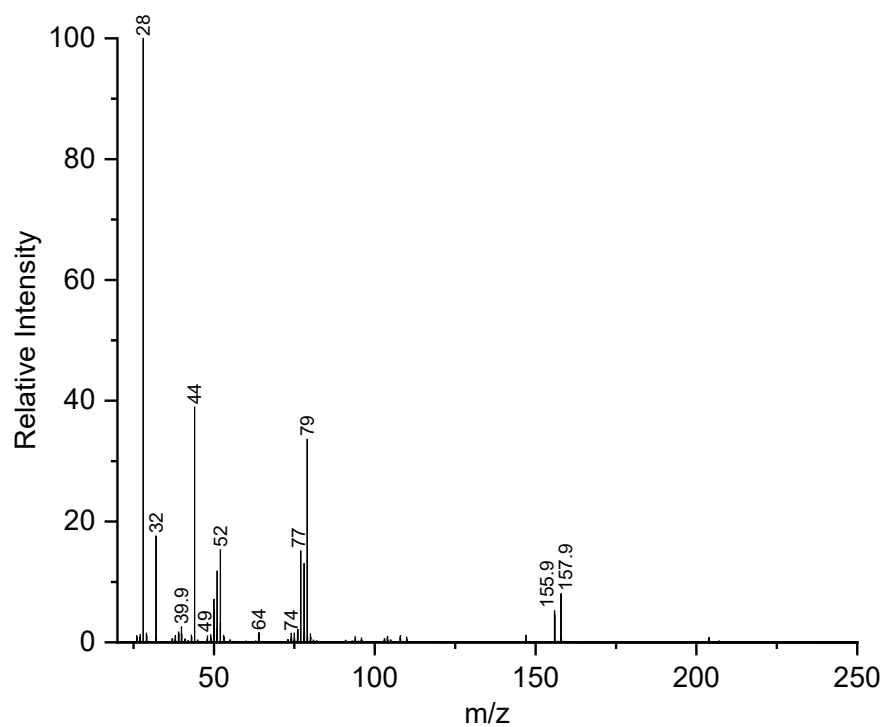
Fig. S13. Electron ionization mass spectrum of Br-edge graphyne volatiles at 290°C.
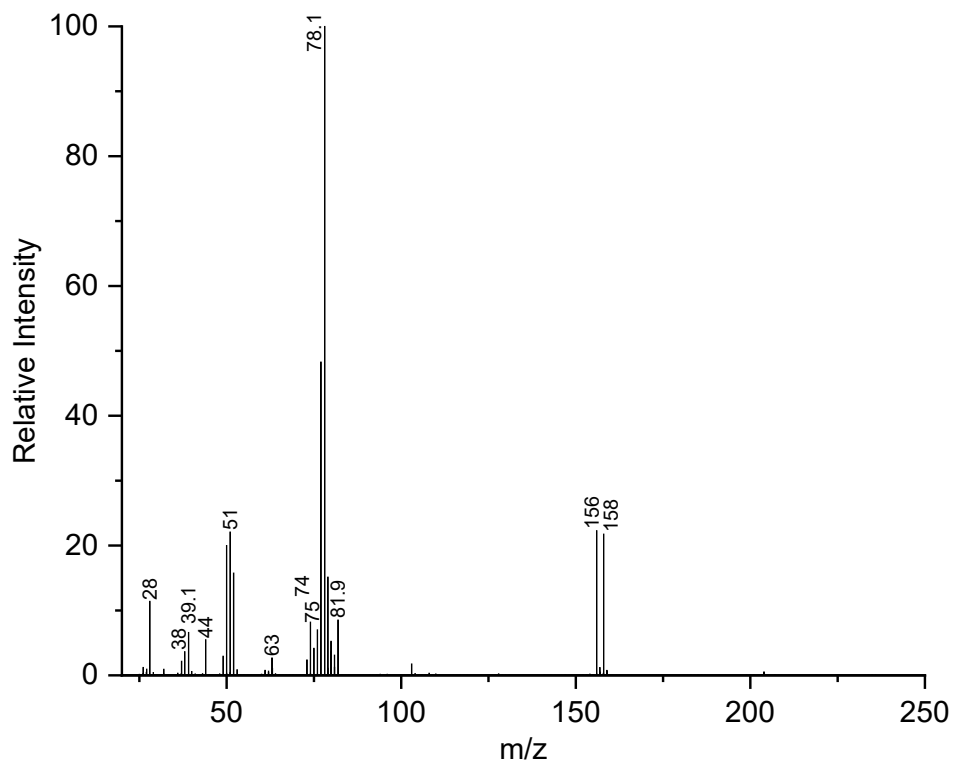
Fig. S14. Electron ionization mass spectrum of Br-edge graphyne volatiles at 350°C.
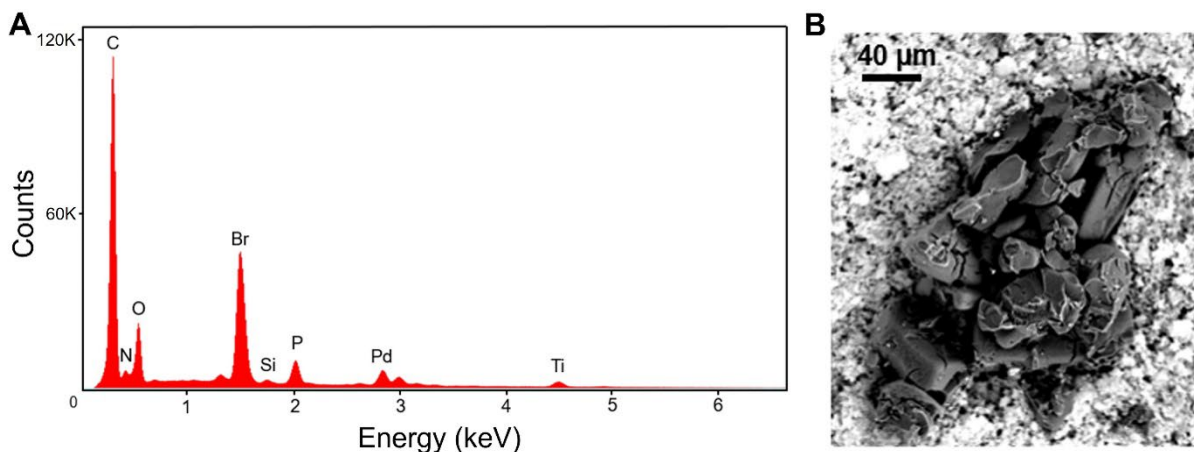
Fig. S15. (*A*) EDX spectrum of the graphyne particles pictured in (*B*). Many graphyne platelets are assembled in the lateral plate direction for the pictured graphyne particles, since electron microscopy on dispersed graphyne indicates that the individual platelets have lateral dimensions of below 300 nm. The peaks in (*A*) are labeled according to the most intense line (K or L) of each identified element. Unlabeled peaks are weaker lines of the already identified elements. The small line at 4.5 keV is associated with the thin metallic titanium layer deposited on the surfaces of particles in order to avoid charging. The above EDX and scanning electron microscope (SEM) image were acquired on a Zeiss Sigma 500 VP using a 10 kV accelerating voltage for the SEM image. Graphyne particles were grounded in silver paste on a gold-coated silicon substrate. To avoid overlap between gold and phosphorous EDX peaks, ~10 nm of titanium was deposited to provide a conductive layer to prevent sample charging. The EDX analysis was performed using APEX™ software to determine atomic and weight percentages.
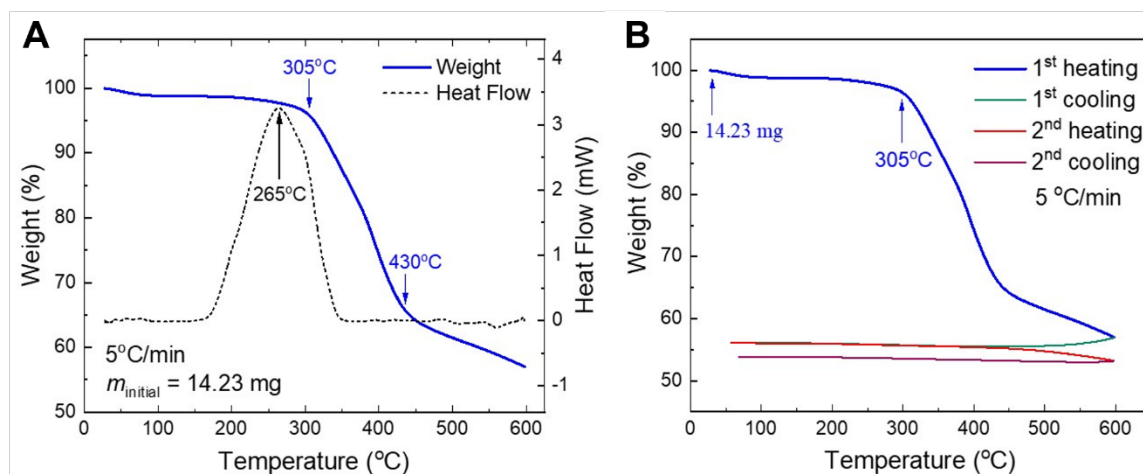
Fig. S16. Comparison of the temperature dependence of (*A*) thermogravimetric weight loss measurements and heat flow measurements (above capacitive baseline) during the first heating of graphyne from near room temperature to 600°C and (*B*) weight loss measurements during this first heating cycle and on subsequent cooling and cooling-heating cycles between these temperatures. The rate of heating and cooling was 5°C/min, and the DTA analysis was in nitrogen gas. The used TA SDT Q600 thermal analyzer enabled simultaneous measurement of weight change (TGA) and heat flow (DSC). Prior to the above measurements, the graphyne was annealed in air for one hour at 65°C in order to largely remove absorbed solvent. Similar

results were obtained for graphyne that was treated at 65°C for 30 minutes in a high vacuum in order to remove solvents before the measurements.
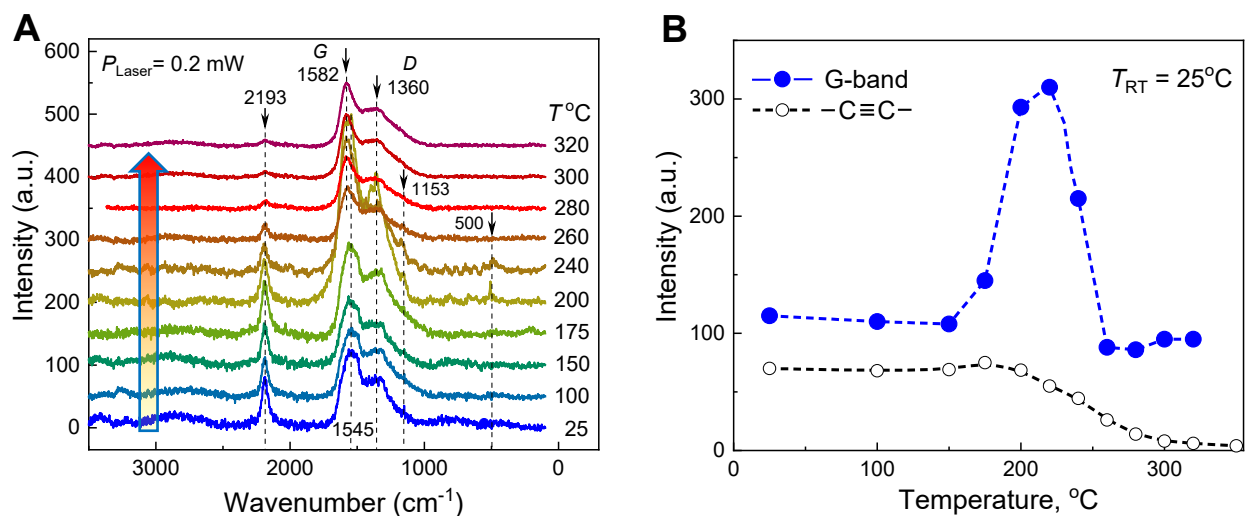
Fig. S17. (*A*) The room temperature Raman spectra (using 532 nm low-intensity excitation) for the initial graphyne (blue curve) and graphyne that was subsequently annealed at progressively higher temperatures for 1 hour in 0.1 mTorr vacuum. All measurements for 10 consecutive annealing temperatures were done for the same local point on a 200x200x50 μm³ particle. For clarity, the spectra for different annealed temperatures are shifted along the y-axis to minimize spectra overlap. (*B*) The dependencies of G-band and triple-bond vibration intensities upon thermal annealing for one hour at each progressively increased temperature. The decrease in G-band Raman intensity for temperatures above 220°C is explained in the next supplemental figure.
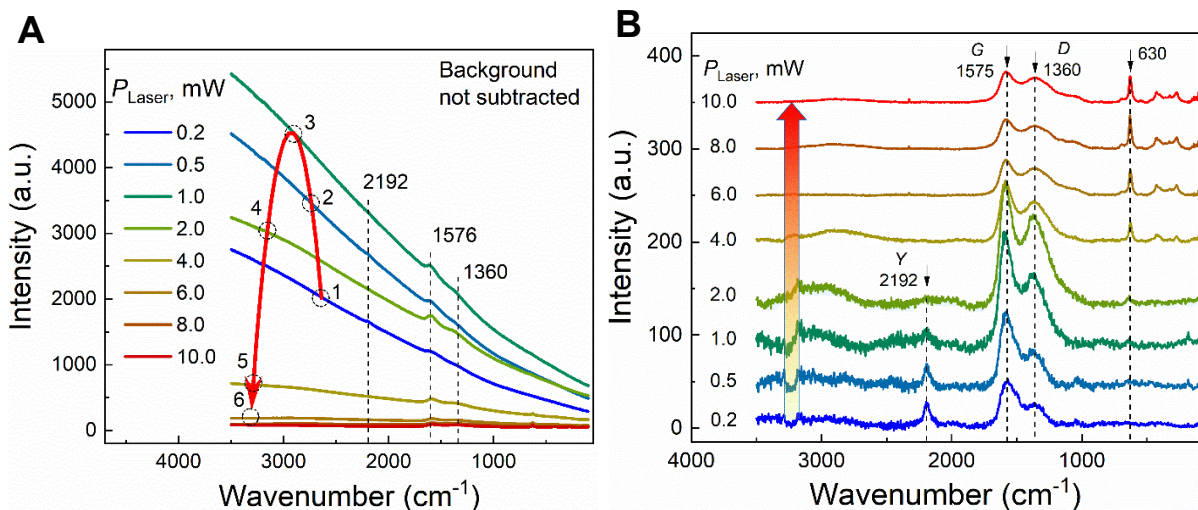
Fig. S18. Raman spectra collected in air for pristine graphyne using increasing power of the laser beam (532 nm) and fixed exposure time for each next measurement (~11 minutes, corresponding to 128 5-s scans). Each measurement was performed at the same exposure site using an aperture of 50 μm and a lens magnification of X10. (*A*) The original raw-data plots without subtraction of the background. The linear

increase of scattering signal towards higher wavenumbers, which is largely due to the background, is caused by the Rayleigh scattering of nanoparticles, which we also observed for nanodiamond and graphdiyne reference powders. The peaked red curve illustrates the radiation intensity-induced change in background scattering. (*B*) The spectra of (*A*) with subtracted background. For clarity, the spectra for different laser powers are shifted along the y-axis. For a laser power of 0.2 mW, the initial spectrum (blue line) did not change by more than ± 5% during 120 minutes of exposure. However, excitation at 0.5 mW laser power gradually shifts the slope of Raman intensity curve 1 towards curve 2 and reduces the triple-bond peak by 7-10 % after 11 minutes of scan collection. The 1 mW laser beam shifts curve 2 towards curve 3 (green line) and further reduces the triple-bond peak. However, the G and D peaks remain almost constant for 0.2 and 0.5 mW beam powers and start to gradually increase for laser powers from 1 to 2 mW. For $P_{Laser} > 1.0$ mW the background decreases, apparently due to volatilization of impurities and the radiation-induced bandgap closure of graphyne (decreasing the laser-beam penetration depth). Correspondingly, the higher beam power reduced the intensities of the G and D peaks.
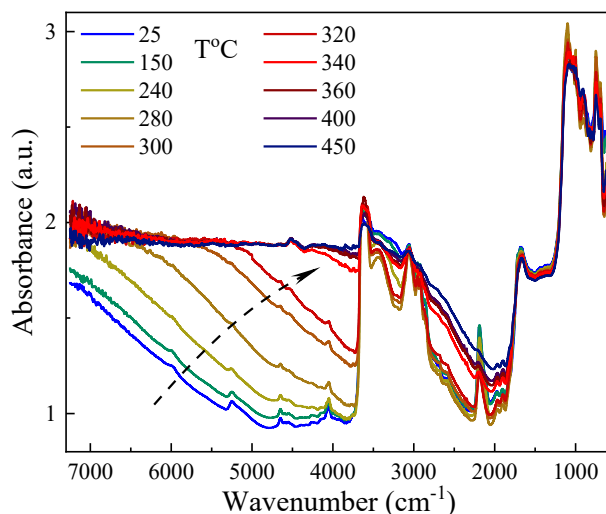
Fig. S19. The room temperature spectra of IR absorbance spectra for graphyne that was annealed in high vacuum (0.1 mTorr) for 1 hour at progressively higher temperatures. The measurement parameters were: 50x50 μm² aperture, 4 cm⁻¹ resolution, and 10 consecutive scans. The dashed arrow line shows the red shift of the plasmonic edge that is responsible for the derived band gap in Fig. 1A (bottom panel).
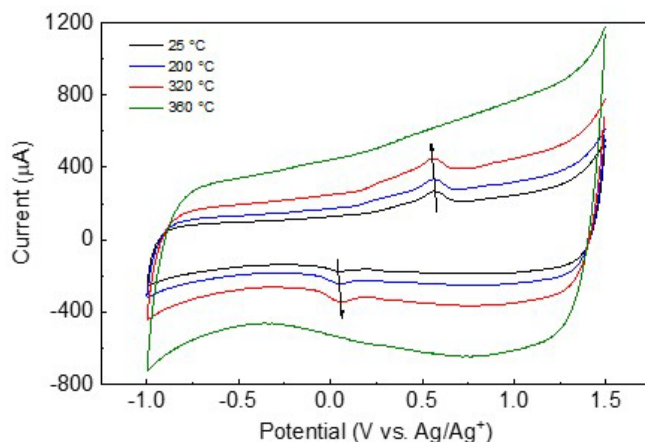
Fig. S20. Illustrative CV spectra for graphyne that was spray coated on a very low areal density forest-drawn MWNT aerogel sheet as the working electrode and then annealed for one hour in a vacuum at progressively increasing temperature before cyclic voltammetry was conducted at room temperature after each annealing step. The spray coating was by graphyne dispersed in dimethylformamide. The electrolyte was 0.1 M tetrabutylammonium hexafluorophosphate in acetonitrile and a high-surface-area Pt counter electrode and an Ag/Ag+ reference electrode were deployed. While these CV spectra show that the CV redox peaks increase with thermal annealing until they vanish as the annealing temperature increases, the ratio of redox peak intensity to overall capacitance decreases with increasing temperature thermal annealing. This capacitance increase results from diffraction-indicated sheet wrinkling that originates from strains between reacted and unreacted graphyne sheet regions during the graphyne transformation, which likely increases the available surface area for both non-Faradaic and Faradaic capacitance.
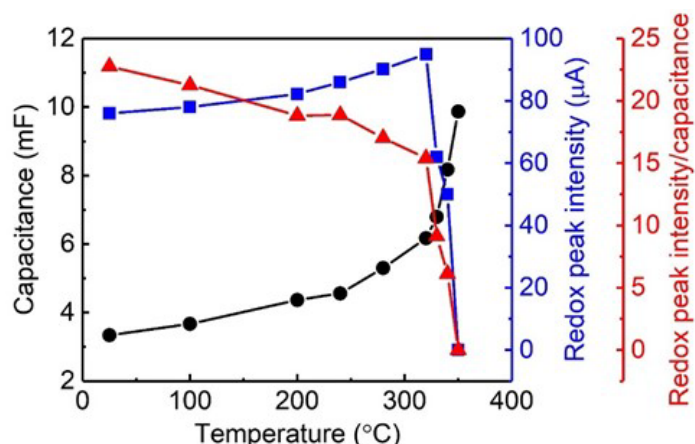
Fig. S21. The room temperature electrochemical cyclic voltammetry capacitance, redox peak height (measured at positive potentials), and the ratio of redox peak intensity to the total electrode capacitance for graphyne that has been annealed in vacuum for an hour at progressively higher temperatures, as a function of the maximum annealing temperature. The 12.5% decrease in the redox peak height to capacitance ratio at below 200°C might be due to the removal of volatiles, especially if their removal affects double-layer capacitance more than redox capacitance.

29
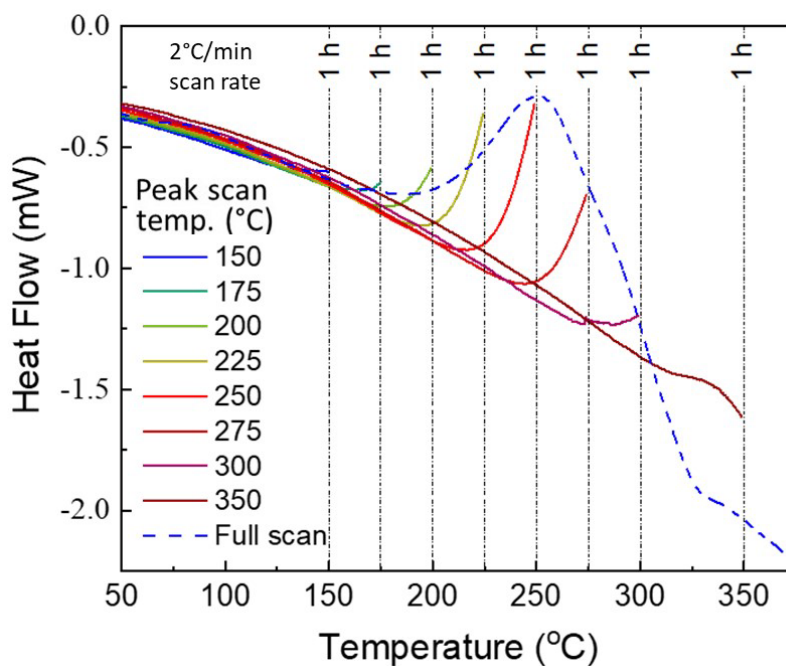
Fig. S22. Measurements for characterizing the kinetics of graphyne transformation. Using a 2ºC/min. heating rate and a very fast cooling rate, the DSC-measured heat flow was measured for 9.80 mg of graphyne powder that was heated to a temperature that is soon after the beginning of the graphyne transformation, annealed at this temperature for one hour, and then cooled back to 40ºC. Afterwards, the same cycle of heating and cooling was conducted numerous times for this graphyne sample using a progressively 25ºC higher annealing temperature than for the last one-hour annealing temperature. The blue-dashed line is for a single uninterrupted full-range scanning measurement using the same heating rate of 2ºC /min.
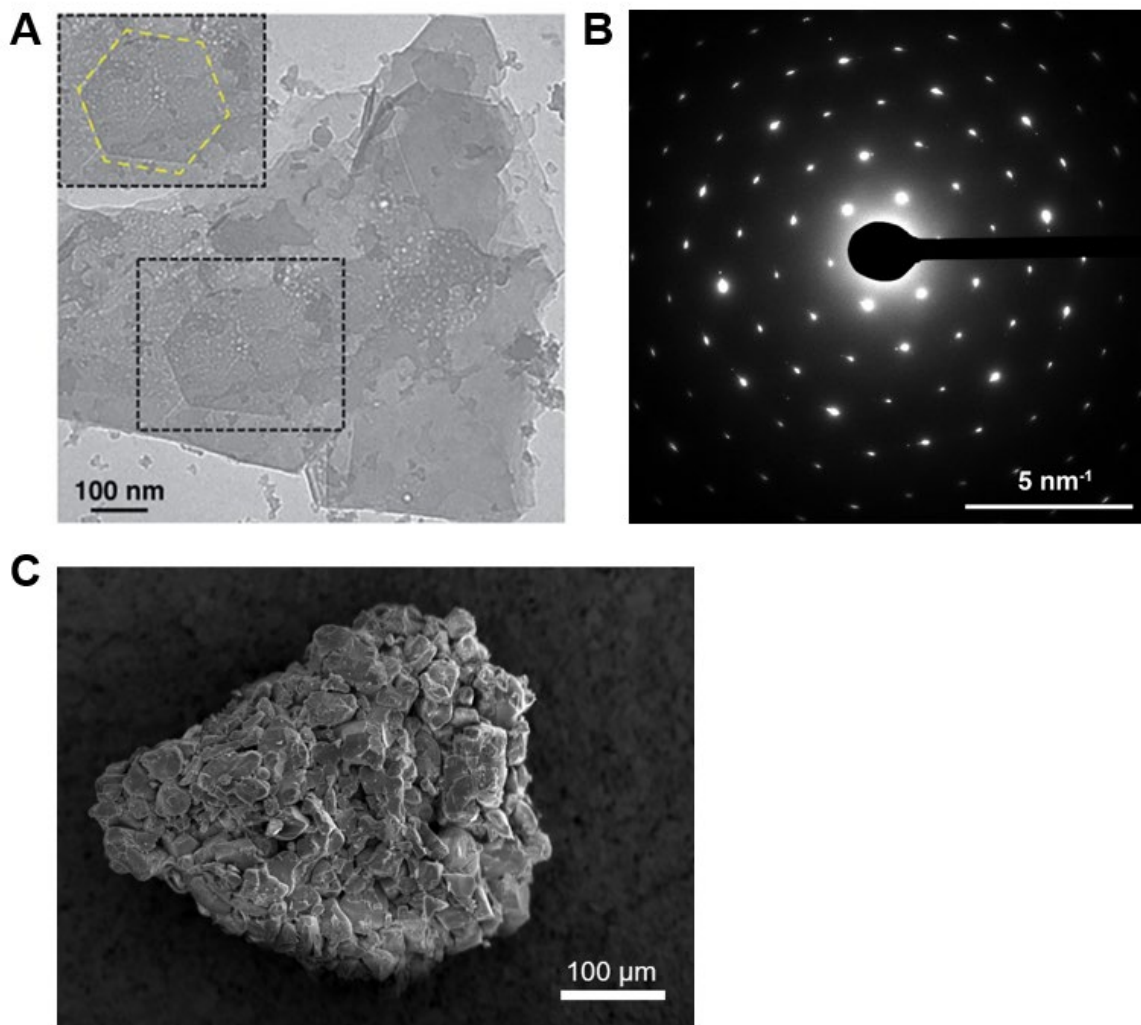
Fig. S23. The size of individual non-reacted stacked graphyne plates, the typical electron pattern from these individual plate stacks, as well as an SEM image of a large graphyne particle. (**A**) Bright field TEM image of an unreacted graphyne sheet stack, from our graphyne synthesis paper (*7*). This and other collected TEM images suggest that the largest sheet dimension of non-aggregated sheet stacks is about 300 nm. (**B**) Presently collected electron diffraction image, which is basically the same as we provided in (*7*). (**C**) SEM image of a typical large graphyne particle that is a poorly ordered aggregate of an enormous number of individual graphyne plates, which was gold-coated to minimize charging. Even the small dimension particles in this image are typically much wider than the individual graphyne sheet stacks that we found in electron diffraction images.

AA Stacking

AB1 Stacking

AB2 Stacking
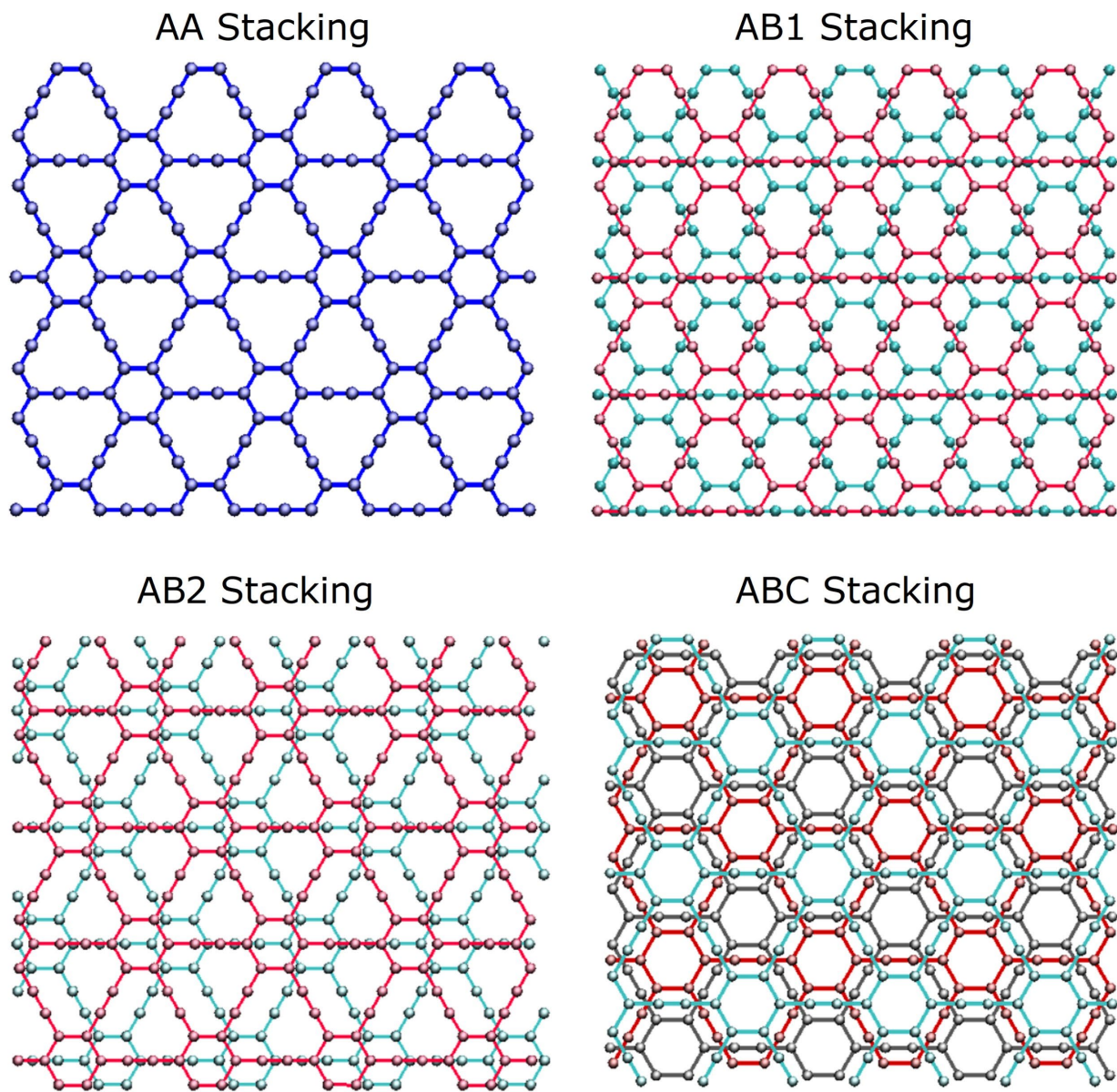
ABC Stacking

Fig. S24. Orthogonal to sheet plane views of AA, AB1, AB2, and ABC stacking arrangements for graphyne. Only the AA and AB1 packing modes are consistent with the interplanar reaction of triple bonds to form polyacetylene chains in reacted graphyne.
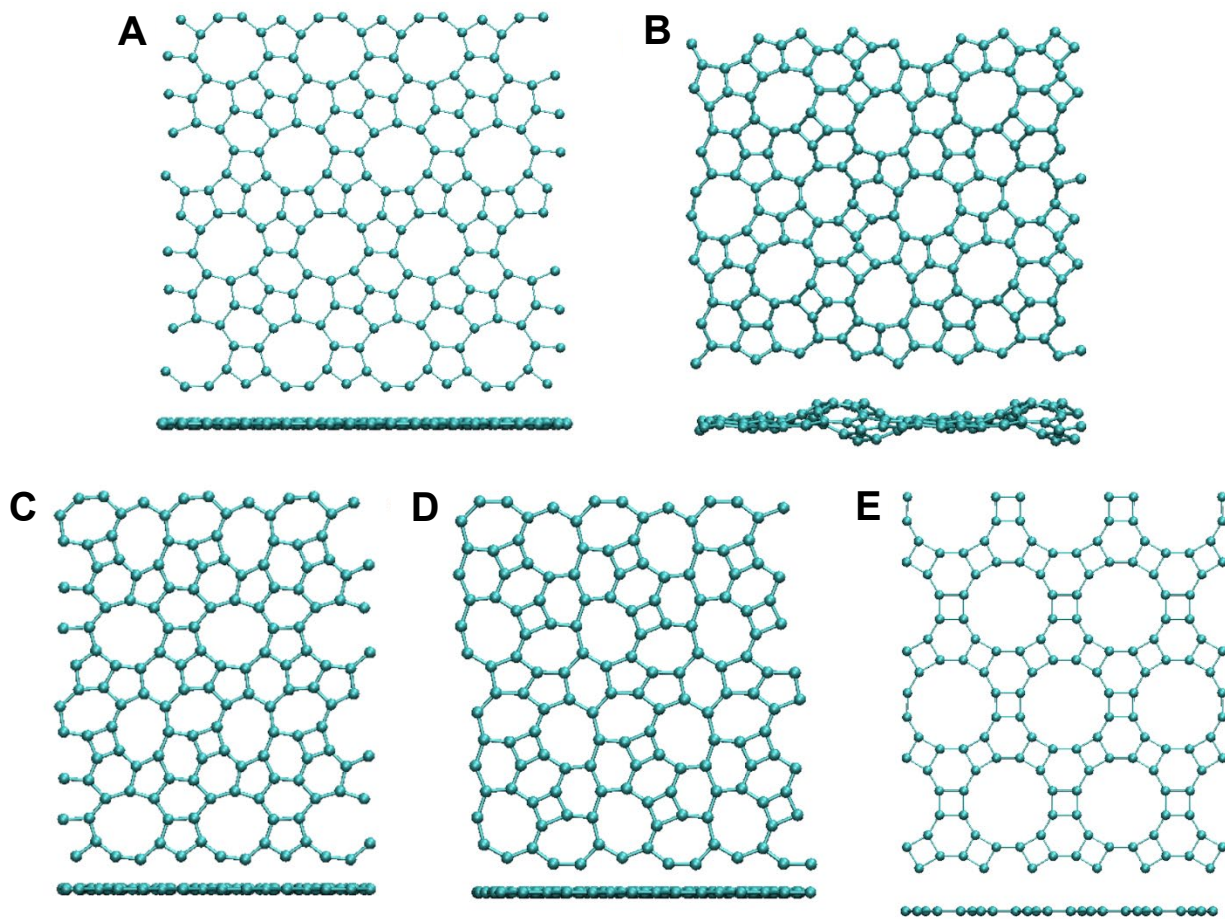
Fig. S25. Upper (top) and lateral views (bottom) of the ReaxFF-MD optimized atomic geometries of the predicted 2D carbon products from in-plane Bergman-like reactions. These structures are for (*A*) 5,6,9 ringene, (*B*) 4-9 ringene, (*C*) 4-9 double ringene, (*D*) 4-8 ringene, and (*E*) biphenylene. The so-called biphenylene (E) has been previously investigated.
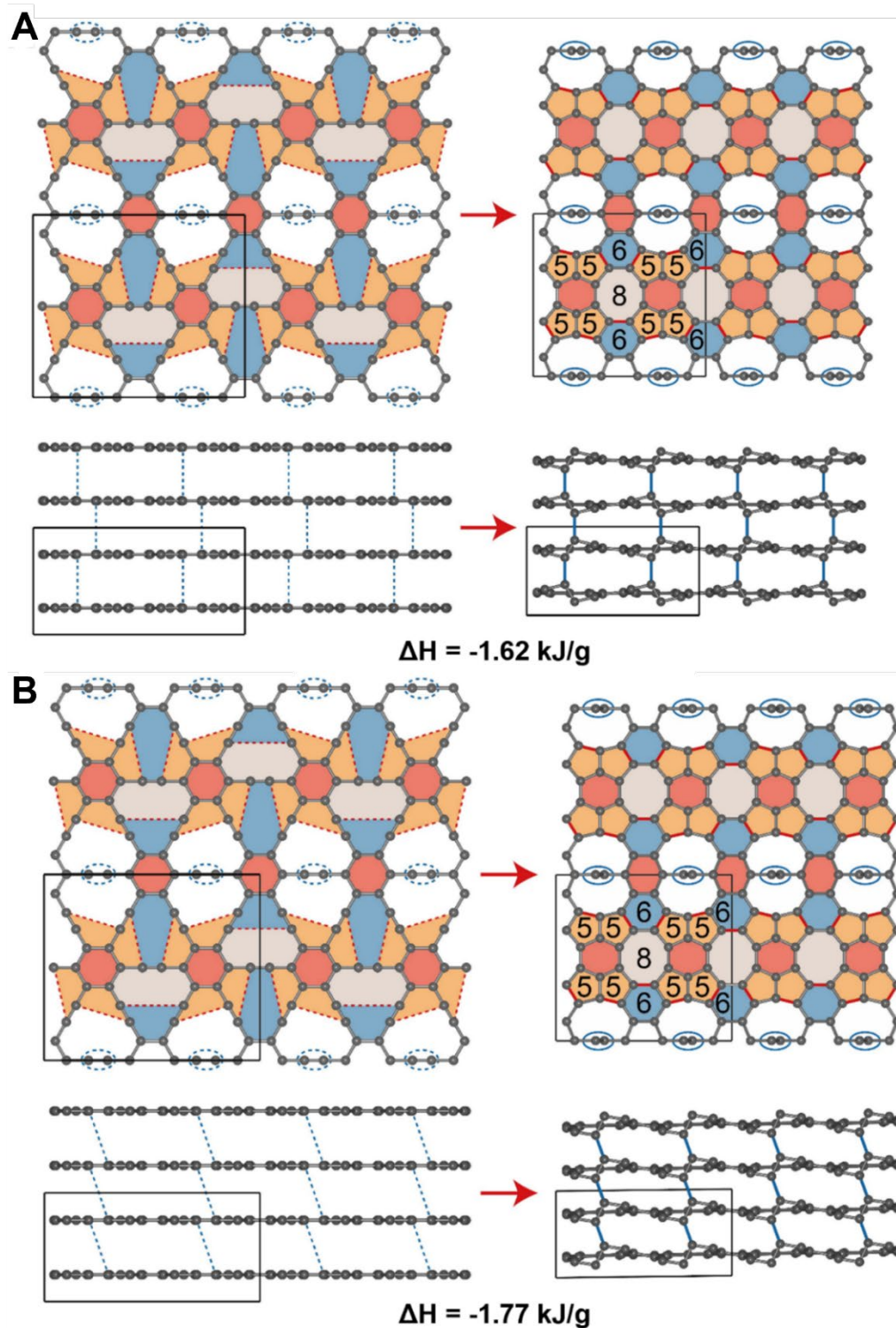
Fig. S26. Two possible transformations that convert an eclipsed AA stacking mode of graphyne to all-sp^2 carbon phases by a sequence of in-plane reaction and cross-plane reaction, without breaking any bond in the original graphyne. The polyene chains in (*A*) and (*B*) are cis and trans, respectively. Only one-fifth of the acetylenic carbons react inter-layer by forming polyacetylene chains and the rest react intra-layer by forming new rings.
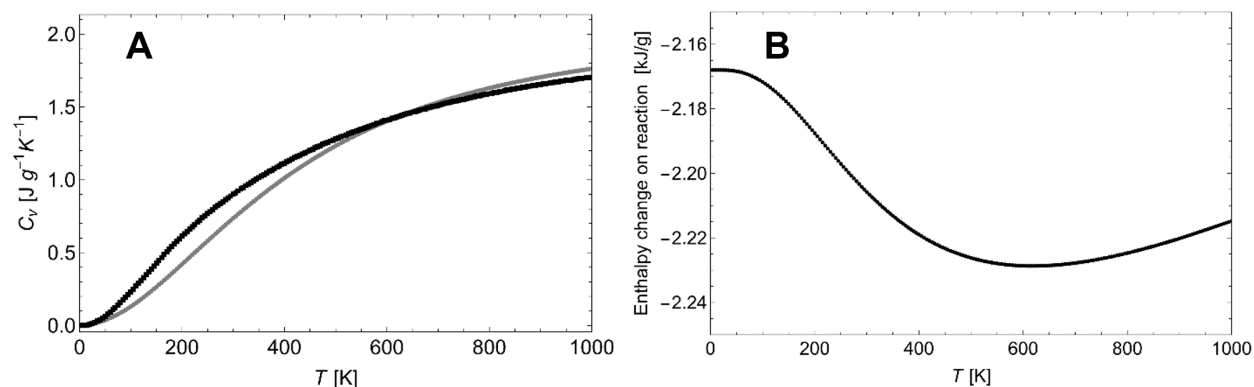
Fig. S27. The theoretically calculated temperature dependence of heat capacitances for (*A*) 5,6,9 ringene (black curve) and unreacted graphyne (gray curve) and (*B*) the corresponding effect of these heat capacities on the enthalpy change of reaction for temperatures in the above curves where graphyne does not react and the especially high temperatures where the reacted graphyne volatilizes. (*A*) The Quantum Expresso calculated constant-volume heat capacities of periodically stacked sheets of graphyne (gray curve) and 5,6,9 ringene (black curve) as a function of temperature when ignoring higher temperature graphyne sample reaction, as well as reacted graphyne volatilization at extreme temperatures. In fact, much of the entire sample will evaporate in a vacuum by 600°C. (*B*) The thereby calculated temperature dependence of enthalpy change between the above parent and product states, which are valid only below the above indicated temperatures. Although the 0 K calculated enthalpy difference (-2.17 kJ/g) was for a Quantum Expresso calculation, ReaxFF potential and VASP calculations (-1.84 and -2.21 kJ/g, respectively) provided similar results.

Table S1. Comparison of synchrotron-diffraction interplanar spacings (d) for previously investigated and presently investigated unreacted graphyne with the d spacings derived for the previously determined (8) electron-diffraction-derived hexagonal unit cell and the theoretically calculated unit cell. Because of long-range disorder in inter-layer stacking, only (h,k,0) and (0,0,l) reflections are observed, and the chosen c-axis axial lengths are the measured and calculated inter-sheet spacings. Since reliable inter-sheet spacings were not determined by electron diffraction, no (0,0,l) spacings are reported for the electron diffraction data. The electron-diffraction-derived hexagonal unit cell hexagonal unit cell has a = 6.88 Å. Also, while the theoretically calculated inter-planar spacing slightly varies depending upon the assumed 3D structure, only its approximate value (3.4 Å) is reported. The theoretically calculated a-axis length is about 6.88 Å. X-ray diffraction peaks are sometimes not observed because of unfavorable orientation for the investigated powder samples.

h,k,l	$d_{x\text{-ray}}$ (Å), previous	$d_{x\text{-ray}}$ (Å), present	$d_{electron}$ (Å), previous	Theory (Å) at 0K
1,0,0	6.02		5.96	5.96
0,0,1	3.48	3.41		3.4
1,1,0	3.44		3.44	3.44
2,0,0	3.01	3.07	2.98	2.98
1,2,0	2.64	2.63		

Table S2. Atomic and weight percent composition from *SI Appendix*, Fig. S15. The palladium content of graphyne measured in several samples is less than one atomic percent.

Element	C	Br	Pd	O	P	N	Si	Cu	I
Atomic %	85.7	3.0	0.9	6.4	5.8	2.9	0.1	< 0.1	< 0.1
Weight %	66.4	15.5	6.4	5.8	2.9	2.9	0.1	< 0.1	< 0.1

Table S3. The density and formation energies calculated by DFT for the investigated stacking modes of graphyne.

Stacking structure	Density [g/cm³]	Energy [eV/atom]	Difference from the most favorable energy structure
AA	1.636	-7.4354	+9.9 meV/atom (79 J/g)
AB1	1.743	-7.4447	+0.5 meV/atom (4 J/g)
AB2	1.753	-7.4453	0 meV/atom (0 J/g)
ABC	1.749	-7.4462	-0.9 meV/atom (-7 J/g)

Table S4. The density, formation energy, and energy differences with respect to the non-bonded AB2 stacking of graphyne structures and the relative percentage of shrinking along all directions for 2-cis, 1-sp polygraphyne; 2-trans, 1-sp polygraphyne; 3-cis polygraphyne; 1-cis, 2-trans polygraphyne; and 3-trans polygraphyne, as well as for Hex-C24. Values obtained from MD ReaxFF potential energy minimizations are in black and those from DFT calculations, which are likely more reliable, are in blue.

Structure	Density [g/cm³]	Energy [eV/atom]	Energy [10¹ kJ/g]	$E_{BONDED} - E_{NON-BONDED}$ [eV/atom] (kJ/g)	$(L_{BONDED} - L_{NON-BONDED})/L_{NON-BONDED}$ along X (Y) [Z] direction
Non-bonded AB2	1.799 1.753	-6.903 -7.445	-5.545 -5.971	0 0	0
2-cis, 1-sp polygraphyne	2.400 2.423	-7.049 -7.477	-5.663 -5.997	-0.146 (-1.173) -0.032 (-0.257)	-0.2% (-2.34%) [-24.1%] -1.23% (-3.33%) [-24.2%]
2-trans, 1-sp polygraphyne	2.419 2.417	-7.072 -7.518	-5.681 -6.030	-0.168 (-1.350) -0.073 (-0.585)	-0.52% (-6.28%) [-22.3%] -0.92% (-5.41%) [-22.6%]
3-cis polygraphyne	2.439	-7.144	-5.739	-0.241 (-1.940)	-1.40% (-1.38%) [-26.1%]
1-cis, 2-trans polygraphyne	2.550 2.559	-7.207 -7.591	-5.789 -6.088	-0.304 (-2.442) -0.145 (-1.163)	-6.24% (-4.11%) [-23.5%] -5.78% (-4.34%) [-24.0%]
3-trans polygraphyne	2.544 2.616	-7.231 -7.604	-5.809 -6.099	-0.328 (-2.635) -0.159 (-1.275)	-5.70% (-6.78%) [-21.6%] -6.44% (-5.85%) [-23.4%]
Hex-C24	2.766 2.771	-7.353 -7.871	-5.907 -6.313	-0.450 (-3.615) -0.426 (-3.417)	-0.97% (-1.15%) [-35.2%] -0.08% (+0.06%) [-36.8%]

Table S5. The formation energies and relative percentages of shrinking along sheet directions for pristine graphyne and four possible intra-sheet reaction products calculated using the MD ReaxFF potential (in black) and DFT calculations (in blue). The energy differences were calculated with respect to a pristine layer of graphyne. The A-D structures are labeled in Fig. 4 and *SI Appendix*, Fig. S23 and the biphenylene structure is also shown in *SI Appendix*, Fig. S23. The below X and Y directions are for the orthogonal cells shown in Fig. 4, where the pictured orthogonal cells have DFT-calculated a-axis and b-axis sheet-plane values at 0°K of 6.882 and 11.921 Å for graphyne, 5.914 and 11.465 Å for 5,6,9 ringene, and 6.119 and 11.039 Å for 4-9 double ringene. Since 4-8 ringene cannot be described by an orthorhombic cell, it is not in the cell length change comparison. The calculated hexagonal unit cell parameter for graphyne is 6.882 Å.

Structure	Energy [eV/atom]	Energy [kJ/g]	Energy difference [eV/atom] (kJ/g)	$(L_{BONDED} - L_{NON-BONDED})/L_{NON-BONDED}$ along X (Y) direction
Pristine	-6.850	-5.503	0	0

	-7.398	-5.933	0	0
A	-7.079 -7.674	-5.687 -6.154	-0.229 (-1.837) -0.276 (-2.214)	-16.3% (-5.88%) -14.1% (-3.82%)
B	-7.003 -7.561	-5.626 -6.064	-0.153 (-1.227) -0.163 (-1.307)	-12.5% (-14.3%) -10.1% (-11.1%)
C	-7.007 -7.557	-5.629 -6.061	-0.157 (-1.259) -0.159 (-1.275)	-14.1% (-9.75%) -11.1% (-7.39%)
D	-6.885 -7.443	-5.531 -5.969	-0.035 (-0.281) -0.045 (-0.361)	
Biphenylene	-6.717 -7.393	-5.396 -5.929	+0.133 (+1.067) +0.005 (+0.040)	-3.02% (-2.97%) -1.61% (-1.61%)

Table S6. The calculated space groups, unit cell parameters, and fractional atomic coordinates of the inter-plane-reacted graphyne structures shown in Fig. 3, labeled by the alphabetic capital letters in this figure. After the space group and unit cell dimensions for each structure, the labels of different independent carbons and their fractional coordinates in the x, y, and z directions are given. Carbons arising from phenyl rings in the original graphyne are specially designated by the term phenyl.

Structure	Space group	a (Å)	b (Å)	c (Å)	α (°)	β (°)	γ (°)
B. 2-cis, 1-sp polygraphyne	Bmmb	11.5128	6.7913	5.0538	90.000	90.000	90.000
C1 (sp^2)	0.71340	0.47030	0.34875	C2 (phenyl)	0.89228	0.14784	0.78323
C3 (phenyl)	1.00000	-0.45420	0.24590	C4 (sp)	0.50000	-0.33975	0.22996

Structure	Space group	a (Å)	b (Å)	c (Å)	α (°)	β (°)	γ (°)
C. 2-trans, 1-sp polygraphyne	Bmmb	6.8124	11.2657	5.1611	90.000	90.000	90.000

C1 (sp^2)	0.21512	0.02663	0.13927	C2 (phenyl)	0.89772	-0.14031	0.84419
C3 (phenyl)	0.29532	-0.25000	0.34147	C4 (sp)	0.41069	0.25000	0.15772

Structure	Space group	a (Å)	b (Å)	c (Å)	α (°)	β (°)	γ (°)
D. 3-cis polygraphyne	P6$_3$/mcm	6.8221	6.8221	4.7200	90.000	90.000	120.000
C1 (phenyl)	0.00000	0.21088	0.49841	C2 (sp^2)	0.00000	0.41920	0.40116

Structure	Space group	a (Å)	b (Å)	c (Å)	α (°)	β (°)	γ (°)
E. 1-cis, 2-trans polygraphyne	Pbca	12.9561	11.3934	5.0687	90.000	90.000	90.000
C1 (phenyl)	0.82799	0.14276	0.10037	C2 (phenyl)	0.93464	0.14197	0.12582
C3 (sp^2)	0.77114	0.03532	0.01553	C4 (sp^2)	0.73056	0.96344	0.21512
C5 (sp^2)	0.98924	0.02662	0.12477	C6 (phenyl)	0.67425	0.85536	0.13224
C7 (phenyl)	0.72793	0.75050	0.11316	C8 (phenyl)	0.00968	0.74903	0.86804
C9 (sp^2)	0.84315	0.74931	0.11425	C10 (sp^2)	0.89458	0.74994	0.86455
C11 (phenyl)	0.93611	0.14336	0.62496	C12 (sp^2)	0.98888	0.02652	0.62487

Structure	Space group	a (Å)	b (Å)	c (Å)	α (°)	β (°)	γ (°)
F. 3-trans polygraphyne	Fddd	12.8656	22.2830	2.5535	90.000	90.000	90.000
C1 (phenyl)	0.94604	0.55457	0.55193	C2 (sp^2)	0.88800	0.11210	0.11861
C3 (phenyl)	0.85870	0.25000	0.75000	C4 (sp^2)	0.97433	0.25000	0.75000

Table S7. The calculated space groups, unit cell parameters, and fractional atomic coordinates of the in-plane-reacted ringene structures shown in Fig. 4 and *SI Appendix*, Fig. S23. These structures are for effectively infinitely separated sheets, since eclipsed sheets are periodically translated from each other by 40 Å in the c-axis direction. After the space group and unit cell dimensions for each structure, the labels of different independent carbons and their fractional coordinates in the x, y, and z directions are given. Since all carbons become part of sp^2 carbon rings, those arising from phenyl rings in the original graphyne are specially designated by the term phenyl.

Structure	Space group	a (Å)	b (Å)	c (Å)	α (°)	β (°)	γ (°)
A. 5,6,9 ringene	P2/m	5.914	11.465	40.000	90.000	90.000	89.194
C1 (sp^2)	0.69814	0.25964	0.50000	C2 (sp^2)	0.37261	0.85869	0.50000
C3 (phenyl)	0.71046	0.46955	0.50000	C4 (phenyl)	0.32886	0.40326	0.50000
C5 (phenyl)	0.21591	0.05490	0.50000	C6 (phenyl)	0.97615	0.87136	0.50000
C7 (phenyl)	0.82573	0.06703	0.50000	C8 (phenyl)	0.43495	0.63058	0.50000
C9 (sp^2)	0.95815	0.25081	0.50000	C10 (sp^2)	0.90963	0.64861	0.50000
C11 (sp^2)	0.54797	0.93862	0.50000	C12 (sp^2)	0.05690	0.55158	0.50000

Structure	Space group	a (Å)	b (Å)	c (Å)	α (°)	β (°)	γ (°)
B. 4-9 ringene	P1	12.379	10.600	40.000	87.922	84.286	90.290
C1 (sp^2)	0.33082	0.25374	0.49803	C2 (sp^2)	0.88768	0.28280	0.50681
C3 (sp^2)	0.12252	0.77602	0.49608	C4 (sp^2)	0.52157	0.75307	0.50505
C5 (sp^2)	0.44258	0.25499	0.49851	C6 (sp^2)	0.81127	0.18169	0.49830
C7 (sp^2)	0.23190	0.75111	0.49942	C8 (sp^2)	0.63255	0.73214	0.50818
C9 (phenyl)	0.37677	0.45738	0.50477	C10 (phenyl)	0.87899	0.51815	0.52535
C11 (phenyl)	0.17353	0.39702	0.50195	C12 (phenyl)	0.73027	0.39424	0.52324
C13 (phenyl)	0.08788	0.04081	0.49067	C14 (phenyl)	0.60402	0.95560	0.49684
C15 (phenyl)	0.39833	0.92208	0.49737	C16 (phenyl)	0.96326	0.88278	0.47751
C17 (phenyl)	0.48555	0.13135	0.49598	C18 (phenyl)	0.88392	0.08653	0.48573
C19 (phenyl)	0.24791	0.61520	0.50247	C20 (phenyl)	0.68658	0.61941	0.51937
C21 (sp^2)	0.00077	0.24443	0.49968	C22 (sp^2)	0.68967	0.18367	0.50161

C23 (sp²)	0.41444	0.70254	0.50514	C24 (sp²)	0.88344	0.70184	0.51296
C25 (phenyl)	0.15680	0.53791	0.50180	C26 (phenyl)	0.65201	0.49299	0.52243
C27 (phenyl)	0.99340	0.11614	0.49020	C28 (phenyl)	0.59829	0.09090	0.49629
C29 (sp²)	0.11291	0.27510	0.50008	C30 (sp²)	0.65832	0.30110	0.51356
C31 (phenyl)	0.35751	0.58498	0.50551	C32 (phenyl)	0.79864	0.61766	0.52466
C33 (phenyl)	0.38476	0.05128	0.49493	C34 (phenyl)	0.87284	0.96798	0.47482
C35 (sp²)	0.33815	0.80451	0.50042	C36 (sp²)	0.88179	0.79011	0.48865
C37 (phenyl)	0.28633	0.37390	0.50171	C38 (phenyl)	0.84372	0.39486	0.52059
C39 (phenyl)	0.06834	0.89934	0.48773	C40 (phenyl)	0.50823	0.88616	0.49911
C41 (sp²)	0.28529	0.13400	0.49571	C42 (sp²)	0.79115	0.87069	0.48466
C43 (sp²)	0.07142	0.63443	0.50208	C44 (sp²)	0.57412	0.39790	0.51367
C45 (sp²)	0.17164	0.13839	0.49577	C46 (sp²)	0.68664	0.85775	0.49818
C47 (sp²)	0.47322	0.38122	0.50465	C48 (sp²)	0.96775	0.61123	0.51503

Structure	Space group	a (Å)	b (Å)	c (Å)	α (°)	β (°)	γ (°)
C. 4-9 double ringene	Pm	6.119	11.039	40.000	90.000	90.000	90.000
C1 (sp²)	0.91265	0.36570	0.50000	C2 (sp²)	0.05071	0.71631	0.50000
C3 (sp²)	0.03163	0.25813	0.50000	C4 (sp²)	0.27169	0.69828	0.50000
C5 (phenyl)	0.73191	0.54257	0.50000	C6 (phenyl)	0.44037	0.36911	0.50000
C7 (phenyl)	0.19330	0.94004	0.50000	C8 (phenyl)	0.80695	0.91504	0.50000
C9 (phenyl)	0.95657	0.12915	0.50000	C10 (phenyl)	0.36084	0.58201	0.50000
C11 (sp²)	0.35060	0.14029	0.50000	C12 (sp²)	0.50384	0.74478	0.50000
C13 (phenyl)	0.28805	0.46705	0.50000	C14 (phenyl)	0.15203	0.06480	0.50000
C15 (sp²)	0.29551	0.26086	0.50000	C16 (phenyl)	0.57088	0.62250	0.50000
C17 (phenyl)	0.76841	0.04854	0.50000	C18 (sp²)	0.59295	0.85653	0.50000
C19 (phenyl)	0.68107	0.41054	0.50000	C20 (phenyl)	0.00902	0.85414	0.50000
C21 (sp²)	0.53115	0.06126	0.50000	C22 (sp²)	0.05929	0.47182	0.50000
C23 (sp²)	0.43163	0.94457	0.50000	C24 (sp²)	0.95087	0.58630	0.50000

Structure	Space group	a (Å)	b (Å)	c (Å)	α (°)	β (°)	γ (°)
D. 4-8 ringene	P2/m	6.307	10.786	40.000	90.000	90.000	95.520

C1 (sp^2)	0.72023	0.30795	0.50000	C2 (sp^2)	0.06720	0.70639	0.50000
C3 (phenyl)	0.73492	0.54688	0.50000	C4 (phenyl)	0.42877	0.37889	0.50000
C5 (phenyl)	0.20375	0.94894	0.50000	C6 (phenyl)	0.82006	0.91469	0.50000
C7 (phenyl)	0.98182	0.14501	0.50000	C8 (phenyl)	0.35665	0.57371	0.50000
C9 (sp^2)	0.40118	0.14268	0.50000	C10 (sp^2)	0.50872	0.74164	0.50000
C11 (sp^2)	0.55835	0.05702	0.50000	C12 (sp^2)	0.04480	0.43483	0.50000

Table S8. The DFT calculated electronic bandgaps for the ringene structures shown in Fig. 4 and *SI Appendix*, Fig. S23.

Structure	Bandgap [eV]	Band character
A. 5,6,9 ringene	0	
B. 4-9 ringene	0.1009	Direct
C. 4-9 double ringene	0.2324	Direct
D. 4-8 ringene	0.1748	Indirect

SI References

1. A. S. Mazur, M. A. Vovk, P. M. Tolstoy, Solid-state ^{13}C NMR of carbon nanostructures (milled graphite, graphene, carbon nanotubes, nanodiamonds, fullerenes) in 2000–2019: a mini-review. *Fullerenes, Nanotubes and Carbon Nanostructures* **28**, 202-213 (2019).

2. W. Cai *et al.*, Synthesis and solid-state NMR structural characterization of 13C-labeled graphite oxide. *Science* **321**, 1815-1817 (2008).

3. Kawai, S. *et al.*, Thermal control of sequential on-surface transformation of a hydrocarbon molecule on a copper surface. *Nature Comm.* **7**, 12711 (2016).

4. G. Brunetto *et al.*, Nonzero gap two-dimensional carbon allotrope from porous graphene. *J. Phys. Chem. C* **116**, 12810−12813 (2012).

5. J. -M. Ducéré, C. Lepetit, R. Chauvin, Carbo-graphite: structural, mechanical, and electronic properties. *J. Phys. Chem. C* **117**, 21671-21681 (2013).

6. J. Yun *et al.*, Tunable band gap of graphyne-based homo- and hetero-structures by stacking sequences, strain and electric field. *Phys. Chem. Chem. Phys.* **20**, 26934-26946 (2018).

7. V. G. Desyatkin *et al.*, Scalable synthesis and characterization of multilayer γ-graphyne, new carbon crystals with a small direct band gap. *J. Am. Chem. Soc.* **144**, 17999-18008 (2022).

8. H. Bu, M. Zhao, W. Dong, S. Lu, X. J. Wang, A metallic carbon allotrope with superhardness: a first-principles prediction. *J. Mater. Chem. C.* **2**, 2751-2757 (2014).

9. B. Schuler *et al.*, Reversible Bergman cyclization by atomic manipulation. *Nature Chemistry* **8**, 220-224 (2016).

10. S. Kawai *et al.*, Thermal control of sequential on-surface transformation of a hydrocarbon molecule on a copper surface. *Nature Communications* **7**, 12711 (2016).

11. A. N. Enyashin, A. L. Ivanovskii, Graphene allotrope. *Phys. Status Solidi B* **248**, 1879–1883 (2011).

12. P. Giannozzi *et al.*, QUANTUM ESPRESSO: a modular and open-source software project for quantum simulations of materials. *Journal of Physics: Condensed matter* **21**, 395502 (2009).

13. P. Giannozzi *et al.*, Advanced capabilities for materials modelling with Quantum ESPRESSO. *Journal of Physics: Condensed matter* **29**, 465901 (2017).

14. J. P. Perdew, K. Burke, M. Ernzerhof, Generalized gradient approximation made simple. *Phys. Rev. Lett.* **77**, 3865–3868 (1996).

15. N. Troullier, J. L. Martins, Efficient pseudopotentials for plane-wave calculations. *Physical Review B* **43**, 1993 (1991).

16. M. Ernzerhof, G. E. Scuseria, Assessment of the Perdew–Burke–Ernzerhof exchange-correlation functional. *The Journal of Chemical Physics* **110**, 5029-5036 (1999).

17. J. D. Head, M. C. Zerner, A Broyden—Fletcher—Goldfarb—Shanno optimization procedure for molecular geometries. *Chemical Physics Letters* **122**, 264-270 (1985).

18. A. Togo, I. Tanaka, First principles phonon calculations in materials science. *Scripta Materialia* **108**, 1-5 (2015).